Article

EBV induces CNS homing of B cells attracting inflammatory T cells

https://doi.org/10.1038/s41586-025-09378-0

Received: 20 September 2024

Accepted: 9 July 2025

Published online: 6 August 2025

Check for updates

Fabienne Läderach[1,12], Ioannis Piteros[1,12], Éanna Fennell[1,2], Elena Bremer[1], Mette Last[3], Sandra Schmid[1], Lisa Rieble[1], Caroline Campbell[1], Isis Ludwig-Portugall[4], Lea Bornemann[5], Alexander Gruhl[5], Klaus Eulitz[4], Paul Gueguen[6], Juliane Mietz[7], Anne Müller[1], Gaetana Pezzino[8], Jürgen Schmitz[9], Guido Ferlazzo[8,10,11], Josef Mautner[3] & Christian Münz[1]✉

Epidemiological data have identified Epstein–Barr virus (EBV) infection as the main environmental risk factor for multiple sclerosis, the predominant autoimmune disease of the central nervous system (CNS)[1]. However, how EBV infection initiates multiple sclerosis pathogenesis remains unclear. Here we demonstrate that EBV expands oligoclonal T-bet$^+$CXCR3$^+$ B cells that home to the CNS in humanized mice. Effector memory CD8$^+$ T cells and CD4$^+$ T_H1 cells as well as CD4$^+$ T_H17 cells co-migrate to the brain of EBV-infected humanized mice. T-bet$^+$CXCR3$^+$ B cells can colonize submeningeal brain regions in the absence of other lymphocytes and attract T cells. Depletion of B cells with rituximab or blocking of CXCR3 significantly decreases lymphocyte infiltration into the CNS. Thus, we suggest that symptomatic primary EBV infection generates B cell subsets that gain access to the CNS, attract T cells and thereby initiate multiple sclerosis.

Multiple sclerosis (MS) is the most prevalent chronic neuroinflammatory and demyelinating disease of the CNS[2]. The aetiology of MS involves an interplay between genetic and environmental factors. The most significant genetic factor associated with MS is the human leukocyte antigen (HLA) allele *HLADRB1*15:01* (HLA-DR2b)[3]. Among the environmental components, infection with the human γ-herpesvirus EBV (or HHV4) has long been suspected in MS development and progression[4,5]. Recently, a longitudinal study demonstrated that the risk of developing MS increases 32-fold following EBV infection[1].

The mechanisms by which EBV acts as a trigger of MS pathogenesis are still poorly understood. Defective immune control of EBV infection in B cells that causes CD8$^+$ T cell lymphocytosis during infectious mononucleosis, as well as molecular mimicry between EBV and CNS antigens are suspected to drive MS pathogenesis[6–8]. Although B cells were often thought to be less important than T cells in MS, recent successes of various B cell depletion therapies have highlighted their key role in both the initiation and the progression of MS[9–11]. However, the exact mechanism by which B cells contribute to the development of MS remains unclear.

Atypical B cells (ABCs) are a distinct subset of B cells broadly identified by co-expression of CD19, CD11c, T-bet and variably CXCR3. These cells are often found to be clonally expanded in autoimmune diseases such as systemic lupus erythematosus[12], Sjörgen syndrome[13] and rheumatoid arthritis[14], which also frequently present with elevated EBV titres[15–17]. Recent publications have shown that EBV can infect existing ABCs de novo in vitro[18], and that infection with the distantly EBV-related murine γ-herpesvirus 68 (γHV68) leads to increased proportions of ABCs in mice[19].

Here we present a novel humanized mouse model for EBV infection with expression of the main genetic risk factor for MS, *HLADRB1*15:01* (HLA-DR2b), on both human haematopoietic and mouse stromal cells, which allows us to mimic primary infectious mononucleosis-like EBV infection in vivo. Our data suggest that EBV infection leads to the development of clonally expanded neuroinvasive T-bet$^+$CXCR3$^+$ B cells, which recruit activated and inflammatory T lymphocytes to the CNS. This supports the evidence that EBV causes pathogenic lymphocyte infiltration into the CNS and the subsequent development of MS.

EBV causes lymphocytic CNS infiltration

To investigate whether EBV infection can lead to CNS infiltration of lymphocytes, we reconstituted mice carrying the main genetic risk factor for MS, HLA-DR2b with HLA-DR2b-matched CD34$^+$ HPCs. Specifically, we used BALB/c *Rag2*$^{-/-}\gamma_c^{-/-}$ human SIRPα transgenic *HLADRB1*15:01* knock-in *HLAA*0201* knock-in human β2m knock-in (BRGS-A2DR2) mice. After reconstitution of human immune system components, mice were injected with either 10^5 Raji infectious units of luciferase-encoding B95-8 EBV (EBV-Luc), an EBV strain that was originally isolated from an American patient with infectious mononucleosis[20,21] or with PBS (Fig. 1a). We observed that humanized BRGS-A2DR2 mice showed a faster kinetic of viral titres in the bloodstream and with higher viral loads at 5 weeks post-infection than the more commonly used humanized NOD-*Scid* $\gamma_c^{-/-}$ (NSG) mice (Extended Data Fig. 1a). This supports

[1]Viral Immunobiology, Institute of Experimental Immunology, University of Zürich, Zürich, Switzerland. [2]School of Medicine, Bernal Institute, Health Research Institute, Limerick Digital Cancer Research Centre, University of Limerick, Limerick, Ireland. [3]Institute of Virology, Helmholtz Zentrum München, Munich, Germany. [4]Miltenyi Biotec B.V. & Co. KG, Teterow, Germany. [5]Miltenyi Biotec B.V. & Co. KG, Bielefeld, Germany. [6]Functional Genomics Center, ETH Zurich/University of Zurich, Zurich, Switzerland. [7]Cellular Immunotherapy, Institute of Experimental Immunology, University of Zürich, Zürich, Switzerland. [8]Division of Clinical Pathology, University Hospital Policlinico G.Martino, Messina, Italy. [9]Miltenyi Biotec B.V. & Co. KG, Bergisch-Gladbach, Germany. [10]Department of Experimental Medicine, University of Genoa, Genova, Italy. [11]Unit of Experimental Pathology and Immunology, Istituto di Ricovero e Cura a Carattere Scientifico Ospedale Policlinico San Martino, Genova, Italy. [12]These authors contributed equally: Fabienne Läderach, Ioannis Piteros. ✉e-mail: christian.muenz@uzh.ch

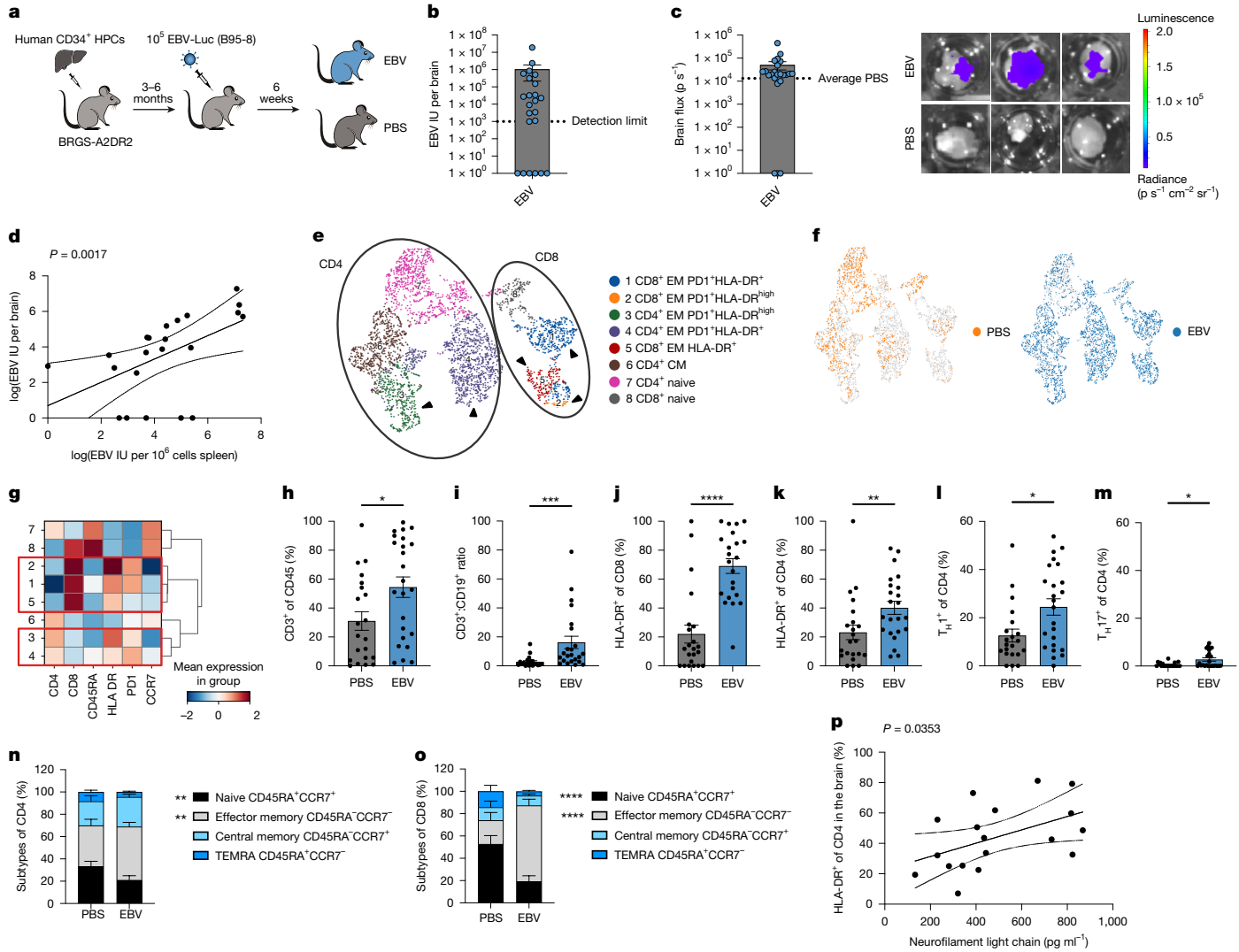

Fig. 1 | EBV infection drives T cell infiltration into the CNS in a new humanized mouse model. a, Schematic illustrating the experimental approach. HPC, haematopoietic progenitor cell. **b**, International units (IU) of EBV viral loads per brain measured by qPCR ($n = 23$). **c**, In vivo bioluminescence measured in flux (p s^{-1}) of perfused brains ($n = 23$) with representative images from EBV-infected and PBS mice. **d**, Correlation between splenic EBV viral load and CNS viral load ($n = 22$). **e**, UMAP visualization of single, live human $CD45^+CD3^+$ T cells. Clusters were manually annotated. The black circles highlight $CD4^+$ and $CD8^+$ T cell populations. CM, central memory; EM, effector memory. Arrowheads indicate clusters 1, 2, and 5 within the $CD8^+$ T cell population and clusters 3 and 4 within the $CD4^+$ T cell population. **f**, UMAP for EBV-infected and PBS mice. **g**, Heatmap depicting mean expression of selected T cell markers in each cluster. The red boxes highlight clusters reduced in PBS mice compared with EBV-infected mice. **h**–**m**, Frequency or ratio of $CD3^+$ (**h**; $P = 0.0175$), $CD3^+$:$CD19^+$ (**i**; $P = 0.0008$), $CD8^+HLA\text{-}DR^+$ (**j**; $P < 0.0001$), $CD4^+HLA\text{-}DR^+$ (**k**; $P = 0.0062$), T_H1 (**l**; $P = 0.0172$) and T_H17 (**m**; $P = 0.0160$) cells ($n = 21$ for PBS and $n = 24$ for EBV). **n**,**o**, Frequency of $CD4^+$ (**n**; $P = 0.002$ for naive and $P = 0.0043$ for effector memory) and $CD8^+$ (**o**; $P < 0.0001$ for naive and $P < 0.0001$ for effector memory) T cell differentiation stages ($n = 21$ for PBS and $n = 24$ for EBV). **p**, Correlation between activated $HLA\text{-}DR^+CD4^+$ T cells in the brain and NfL chain measured in the serum ($n = 18$). Six weeks post-EBV infection, brains were perfused and collected before analysis. Unless otherwise indicated, *P* values were calculated using a two-tailed Mann–Whitney *U* (MWU) test. Data from panels **b**–**o** were generated from five independent experiments with mice reconstituted from six different human $CD34^+$ HPC donors. Panel **p** was generated from three independent experiments with four donors. Panels **d**–**g** were created with crusty.humanitas.it. For correlations, the solid line represents the trend line obtained by linear regression, and the dotted lines indicate the 95% confidence bands. The two-tailed *P* value was calculated using Spearman correlation. For the bar graphs, the error bar indicates the s.e.m; each dot represents one single animal. $^*P < 0.05$, $^{**}P < 0.01$, $^{***}P < 0.001$ and $^{****}P < 0.0001$.

previous observations that EBV replicates to higher viral loads in NSG mice carrying HLA-DR2b-positive, than HLA-DR2b-negative, human immune systems[22]. Transgenic HLA-DR2b introduction did not allow for significant spreading of EBV infection into mouse epithelial cells (Extended Data Fig. 1b). Viral loads were detectable in BRGS-A2DR2 mice as early as 2 weeks post-infection, with viral loads stabilizing around week 4 (Extended Data Fig. 1c). By 6 weeks post-infection, EBV could be detected in perfused brains of infected mice by quantitative PCR (qPCR) and in vivo bioluminescence imaging (Fig. 1b,c). Splenic viral loads by qPCR correlated with those measured in the CNS (Fig. 1d), and luciferase activity correlated with viral loads in perfused brains (Extended Data Fig. 1d). These data suggest that EBV-infected humanized BRGS-A2DR2 mice establish a higher viral load set point than humanized NSG mice and, therefore, more readily allow EBV infection to spread to the CNS.

To investigate which leukocytes carry EBV to the CNS, we analysed the immune cell infiltrates from perfused brains of EBV-infected humanized BRGS-A2DR2 mice by flow cytometry. Although the frequency of $CD19^+$ B cells in the brain did not differ between EBV-infected and PBS mice, (Extended Data Fig. 1g), we observed noticeable changes in the $CD3^+$ T cell compartment in the brains of EBV-infected mice. After manual

gating on human CD45$^+$CD3$^+$ lymphocytes, uniform manifold approximation and projection (UMAP) was used for dimensionality reduction and visualization of the T cell compartment (Fig. 1e,f). EBV infection resulted in the expansion of unique clusters of HLA-DR$^+$PD1$^+$CD8$^+$ or CD4$^+$ effector memory T cells (Fig. 1g and Extended Data Fig. 1e,f). Manual gating confirmed a statistically significant increase in the frequency of CD3$^+$ T cells and HLA-DR$^+$ populations of CD8$^+$ and CD4$^+$ T cells in EBV-infected over PBS mice. We also observed a shift in the T:B cell ratio in the brains of EBV-infected mice. In addition, an increase in total numbers of CD3$^+$ T cells was observed in EBV-infected mice, along with a statistically significant increase in the numbers of activated CD4$^+$ and CD8$^+$ T cells in the brains of EBV-infected mice (Extended Data Fig. 1h–j). The majority of helper T (T_H) cells found in the brain were of the T_H1 subtype in both PBS and EBV-infected mice, with a statistically significant difference between the two groups. Furthermore, the frequency of T_H17 cells was also significantly increased in the brains of EBV-infected mice (Fig. 1l,m).

The expansion of effector memory T cells identified in the UMAP analysis was further confirmed by conventional gating, which showed an increase in the frequency of CD45RA$^-$CCR7$^-$ effector memory T cells when comparing brains of PBS and EBV-infected mice (Fig. 1n,o). Similar trends of T cell activation and differentiation were observed in the spleens of the same mice (Extended Data Fig. 1m,n). To investigate early signs of potential CNS damage, we measured neurofilament light chain (NfL) levels in serum 6 weeks post-infection. A positive correlation between the frequency of activated CD4$^+$ T cells in brains and increased NfL levels in the serum was observed (Fig. 1p). By contrast, the levels of alanine aminotransferase and enzymatic creatinine, which indicate signs of liver or kidney damage, respectively, were not elevated with increased CD4$^+$ T cell activation (Extended Data Fig. 1o,p). Serum NfL levels significantly increased during EBV infection (Extended Data Fig. 1q) and was more pronounced than in PBS mice (Extended Data Fig. 1r). Together, our results indicate that EBV infection, along with the associated T cell differentiation and CD8$^+$ T cell expansion, leads to effector memory CD8$^+$ T cell, T_H1 and T_H17 homing to the CNS.

EBV expands T-bet$^+$CXCR3$^+$ B cells

We next explored whether primary EBV infection can lead to the expansion and enrichment of ABCs in the CNS. Although CD11c is often associated with the ABC phenotype, we found that its expression on CD19$^+$ B cells was not increased following EBV infection (Extended Data Fig. 2a,b), nor did we observe an upregulation of T-bet expression on CD11c$^+$CD19$^+$ cells in the spleen or brain, or an increase in their total numbers after EBV infection (Extended Data Fig. 2c,d). However, we observed significantly elevated frequencies of T-bet$^+$CXCR3$^+$ double-positive CD19$^+$ B cells in the blood, spleen and brain following EBV infection (Fig. 2a–c). In addition, a positive correlation was found between total number of T-bet$^+$CXCR3$^+$ B cells in the spleen and splenic viral loads, indicating that infection drives T-bet$^+$CXCR3$^+$ B cell expansion (Fig. 2d). T-bet$^+$CXCR3$^+$ B cells expressed significantly higher frequencies of CD11c in the blood and spleen but not in the brain than the T-bet$^-$CXCR3$^-$ B cell population. However, this difference was independent of EBV infection status and could also be observed in uninfected mice (Extended Data Fig. 2e,f). To better understand the mechanism by which EBV promotes the expansion of T-bet$^+$CXCR3$^+$ B cells, we sorted uninfected B cells based on their CXCR3 expression. EBV infection of these populations in vitro only minimally induced T-bet expression in CXCR3$^-$ B cells, but rather expanded the T-bet$^+$CXCR3$^+$ population (Extended Data Fig. 2g). Furthermore, although CXCR3^{high} B cells initially had a higher expression of CD11c than the CXCR3^{low} population, this expression was reduced following EBV infection (Extended Data Fig. 2h). EBV-transformed lymphoblastoid B cell lines (LCLs) established from CXCR3$^+$ B cells continued to grow better in culture (Extended Data Fig. 2i).

Next, to assess whether these T-bet$^+$CXCR3$^+$ B cells interact with T cell populations, we performed multiplex immunofluorescence on EBV-infected spleens, which revealed that T-bet$^+$CXCR3$^+$ B cells typically colocalized with CD4$^+$ and CD8$^+$ T cells (Fig. 2e). Characterizing cellular neighbourhoods revealed that T-bet$^+$CXCR3$^+$ B cells were located in areas that were enriched in activated HLA-DR$^+$CD4$^+$ T cells (Fig. 2f). Indeed, a higher frequency of activated HLA-DR$^+$CD4$^+$ T cells was found within the 25 nearest cells to T-bet$^+$CXCR3$^+$ B cells than other B cells (Fig. 2g). EBV infection increased the frequency of T-bet$^+$CXCR3$^+$ B cells, and EBV nuclear antigen 2 (EBNA2) expression was mainly detected in T-bet$^+$CXCR3$^+$ B cells (Extended Data Fig. 3a–c). Using a different staining panel, three neighbourhoods with T-bet$^+$ B cells were identified that contained both activated CD4$^+$ and CD8$^+$ T cells (Extended Data Fig. 3d). All three T-bet$^+$ B cell-containng and activated T cell-containing neighbourhoods were increased in the spleen upon EBV infection (Extended Data Fig. 3e). Expression of the activation marker HLA-DR and the proliferation marker Ki67 in CD4$^+$ T cells was also enriched in proximity (100 µm) to T-bet$^+$CXCR3$^+$ B cells upon EBV infection (Extended Data Fig. 3f–i). T cell activation in the T-bet$^+$CXCR3$^+$ B cell-containing neighbourhoods could also be confirmed by the proliferation marker Ki67 (Extended Data Fig. 3j), and neighbourhoods populated by T-bet$^+$CXCR3$^+$ B cells and proliferating T cells were enlarged in EBV-infected mouse spleens (Extended Data Fig. 3k). Using light-sheet microscopy on cleared brains of EBV-infected humanized mice, clusters of T cell infiltrates were detected in meninges and perivascular regions of the brain parenchyma (Extended Data Fig. 3l). These findings suggest that primary EBV infection drives the expansion of a T-bet$^+$CXCR3$^+$ B cell population in both the periphery and the CNS, and that activated T cells are found in close proximity to these cells and home to perivascular and submeningeal sites in brains of EBV-infected humanized mice.

EBV expanded B cells home to the CNS

To further characterize T-bet$^+$CXCR3$^+$ B cells during EBV infection, we performed single-cell RNA sequencing (scRNA-seq) on CD19$^+$ splenic B cells isolated from EBV-infected humanized BRGS-A2DR2 mice 6 weeks post-infection (Fig. 3a). The results were visualized using UMAP. We recovered five clusters after unsupervised clustering, that we manually annotated as naive B cells, cycling B cells, memory B cells, plasmablasts and plasma cells (Fig. 3b). Co-expression of T-bet (TBX21) and CXCR3 was detected within EBV-infected CD19$^+$ splenocytes (Fig. 3c and Extended Data Fig. 4a). Cells positive for both T-bet$^+$ and CXCR3$^+$ were enriched in the memory B cell compartment (Extended Data Fig. 4b). In addition, T-bet$^+$CXCR3$^+$ cells contained higher frequencies of class-switched immunoglobulin G (IgG). Of note, RNA expression of *IghG1* and *IghG3*, isotypes which are both found to be enriched during EBV infection, colocalized with T-bet$^+$CXCR3$^+$ cells (Extended Data Fig. 4c,d).

B cell receptor (BCR) repertoire sequencing revealed higher clonal expansion of T-bet$^+$CXCR3$^+$ B cells (Fig. 3d,e), even when naive B cells were excluded from the analysis (Fig. 3e). These clonally expanded populations also overlapped with cells expressing the EBV-associated *Wp*/*Cp* EBNA transcript, which encodes all EBNAs. Transcripts encoding the lytic protein BZLF1 and the latent membrane proteins (LMP1 and LMP2A) were also detected in the clonally expanded populations, although at a much lower level (Fig. 3f and Extended Data Fig. 4e). Sequencing further revealed that the majority of EBV-infected B cells are T-bet$^+$ (78.51%; Fig. 3g).

To elucidate the accumulation of T-bet$^+$CXCR3$^+$ B cells in response to EBV infection, we performed a trajectory analysis, which suggested that T-bet$^+$CXCR3$^+$ B cells were progenitors of oligoclonally expanded EBV-infected cells (Fig. 3h,i), which is consistent with our in vitro data demonstrating that T-bet$^+$CXCR3$^+$ B cells mainly emerge from EBV infection of CXCR3$^+$ cells (Extended Data Fig. 2g). This suggests that

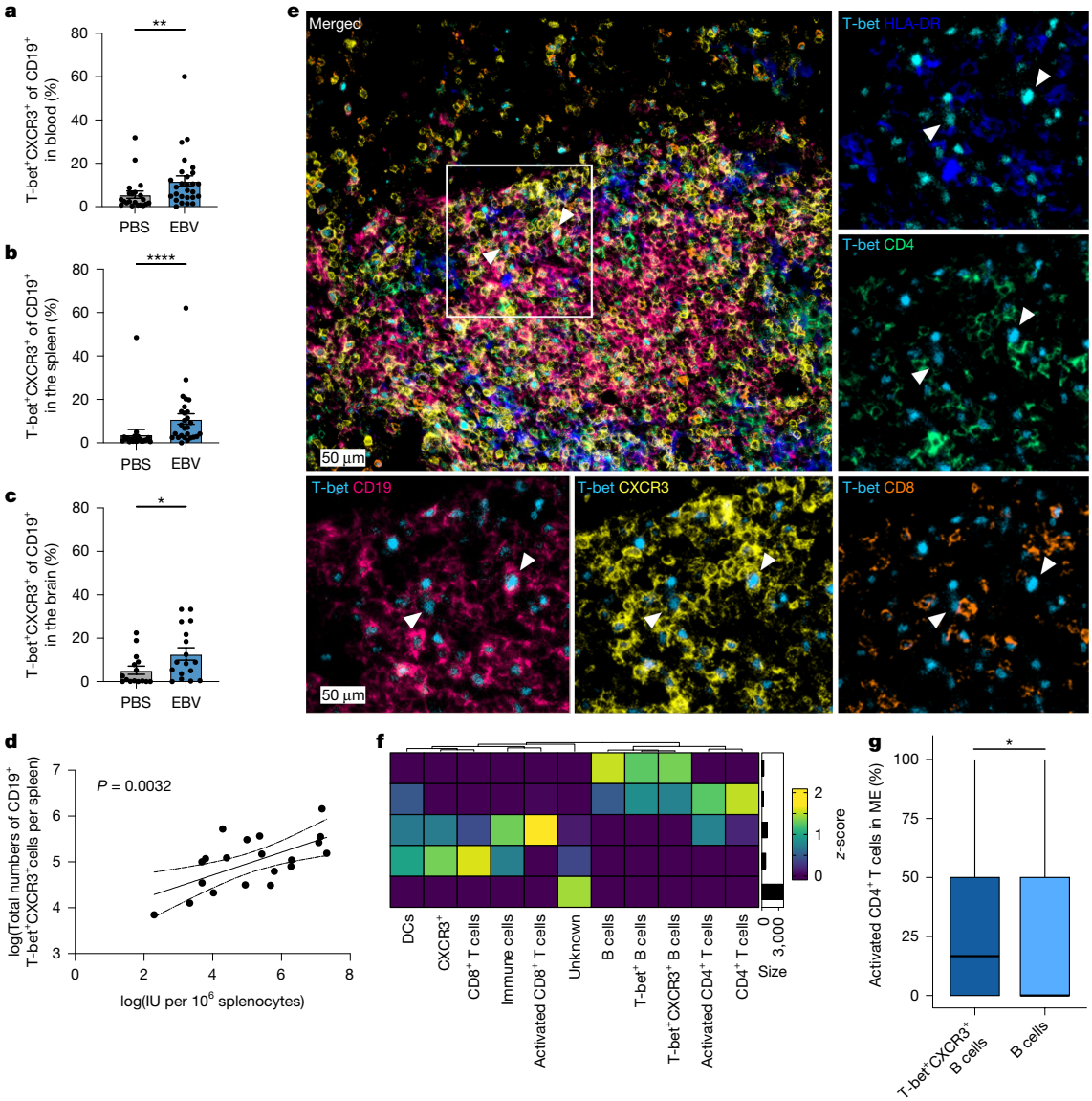

Fig. 2 | EBV infection is linked to T-bet$^+$CXCR3$^+$ B cell expansion. a–**c**, Frequency of CD19$^+$, CXCR3$^+$ and T-bet$^+$ cells in the blood (**a**; $P = 0.0071$; $n = 21$ in PBS and $n = 27$ in EBV), spleen (**b**; $P < 0.0001$; $n = 21$ in PBS and $n = 27$ in EBV) and brain (**c**; $P = 0.0356$; $n = 15$ in PBS and $n = 17$ in EBV) in PBS or EBV-infected mice. **d**, Correlation between the total number of CD19$^+$, CXCR3$^+$ and T-bet$^+$ cells in the spleen and splenic viral loads ($n = 20$). **e**, ChipCytometry co-staining of T-bet with CD19, CXCR3, CD8, CD4 and HLA-DR on the splenic section of EBV-infected mice. The arrowheads indicate identical CD19$^+$T-bet$^+$CXCR3$^+$ B cells. **f**, Quantification of colocalization by neighbourhood analysis identified five neighbourhoods with the indicated cellular contents and neighbourhood size. The *z*-scores of cellular abundances per neighbourhood are displayed. DC, dentritic cell. **g**, Frequencies of activated (HLA-DR$^+$) CD4$^+$ T cells among the 25 nearest cells to T-bet$^+$CXCR3$^+$ B cells versus other B cells ($P = 0.033$; $n = 2{,}568$ B cells and $n = 633$ T-bet$^+$CXCR3$^+$ B cells; microenvironment (ME) of 1 independent experiment). The boxplots define the median value (centre), the interquartile range (25th and 75th percentiles) as the boundaries of the box, and whiskers extend to 1.5 times the 25th and 75th percentiles. Outliers, which lie outside the whiskers, are displayed as individual points. Note that the median value of B cells is 0. Panels **a**,**b**,**d** were generated from five independent experiments with mice reconstituted from six different human CD34$^+$ HPC donors. Panel **c** was generated from four independent experiments with five donors. The *P* values in panels **a**–**c**,**g** were calculated using the two-sided MWU test; the *P* value in panel **d** was calculated by Spearman correlation. For the correlation analysis, the solid line represents the trend line obtained by linear regression, and the dotted lines indicate the 95% confidence bands for which a two-tailed *P* value was calculated. In the bar graphs, the error bar indicates s.e.m.; each dot represents one single mouse. $^*P < 0.05$, $^{**}P < 0.01$ and $^{****}P < 0.0001$.

EBV infection clonally expands pre-existing T-bet$^+$CXCR3$^+$ B cell populations. However, cells with low EBV transcript numbers, either due to reduced gene expression in later stages of latency or early infection, might be falsely annotated as negative. Analysis of the BCR repertoire revealed that the T-bet$^+$CXCR3$^+$ memory B cell population, which was low in EBNA transcripts, shared a high fraction of BCR clones with the cycling B cell and plasma blast populations that were high in EBNA transcripts. This indicates that those T-bet$^+$CXCR3$^+$ cells originate from the EBNA-positive population but might express few, if any, viral transcripts (Extended Data Fig. 4f). Their oligoclonal expansion is supported by pro-proliferative gene expression in EBV-infected and oligoclonally expanded T-bet$^+$CXCR3$^+$ B cells (Extended Data Fig. 4g–j). Similar to our in vitro findings (Extended Data Fig. 2g), T-bet expression was increased in EBV-infected versus uninfected CXCR3$^+$ B cells (Extended Data Fig. 4k).

As CXCR3$^+$ B cells were found abundantly in the CNS of patients with MS[23], we investigated whether potential markers required for B cell infiltration to the CNS[24] were upregulated in T-bet$^+$CXCR3$^+$ cells.

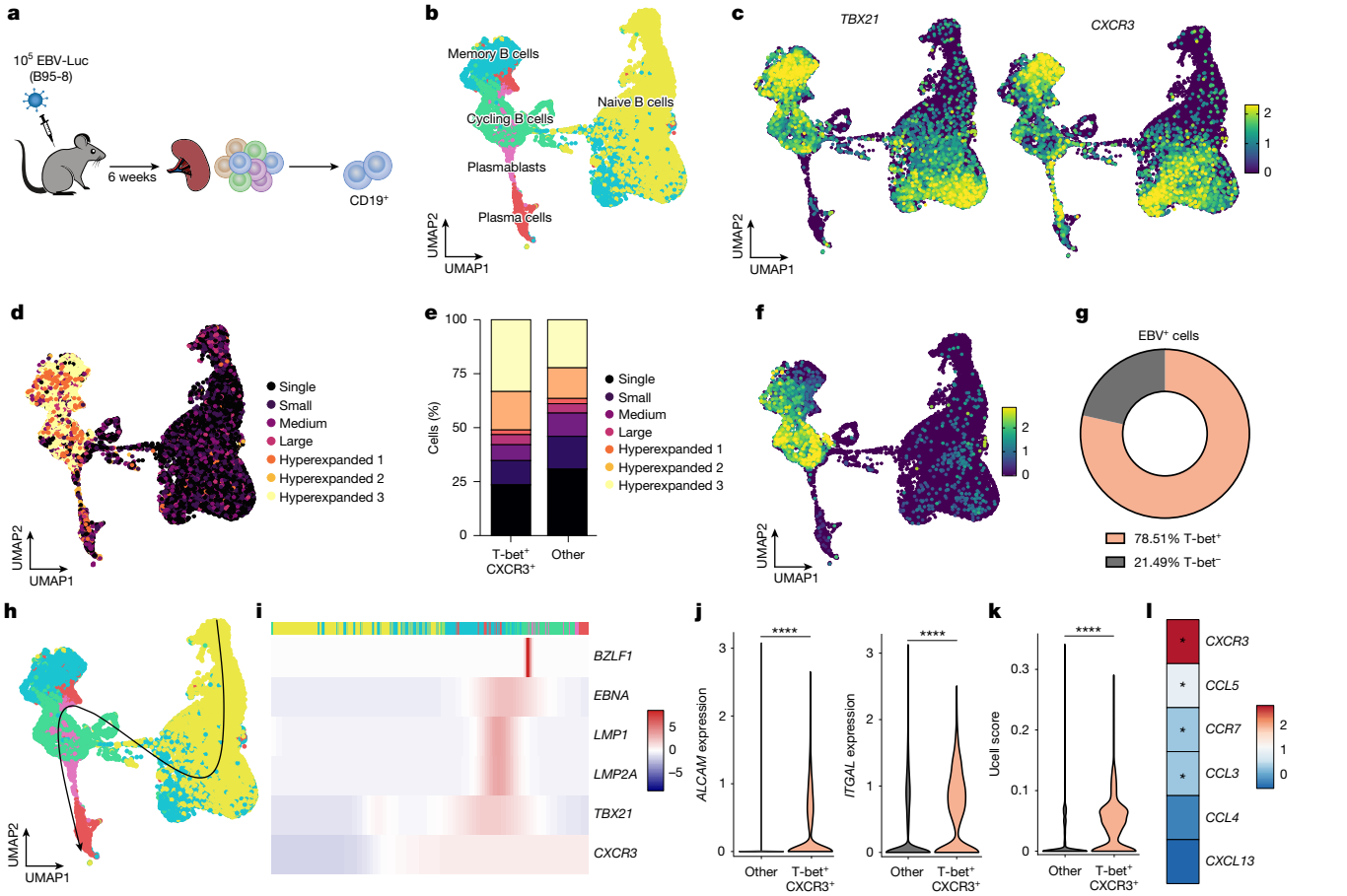

Fig. 3 | EBV infection drives oligoclonal expansion of CNS-homing T-bet$^+$ B cells. a, Schematic illustrating the experimental approach. **b**, UMAP of the sorted CD19$^+$ B cell population. **c**, Expression of the indicated markers. **d**, BCR clonality analysis. Clones were defined by single ($0 < X \leq 1$), small ($1 < X \leq 5$), medium ($5 < X \leq 20$), large ($20 < X \leq 50$) and hyperexpanded 1 ($50 < X \leq 200$). **e**, Stacked bar plots showing clonality distribution within double-positive T-bet$^+$CXCR3$^+$ memory B cells (T-bet$^+$CXCR3$^+$ cells) and double-negative memory B cells (other). **f**, Expression of EBV EBNA transcripts. **g**, Circular chart of T-bet$^+$ and T-bet$^-$ cells within all EBV$^+$ cells. **h**, Trajectory interference by slingshot. **i**, Gene expression of the indicated markers along the slingshot trajectory. **j**, Violin plot of expression of *ALCAM* ($P = 1.30 \times 10^{-20}$) and *ITGAL* ($P = 2.26 \times 10^{-167}$) markers between T-bet$^+$CXCR3$^+$ B cells and other B cells. **k**, Comparison of U cell score of chemotaxis gene set between T-bet$^+$CXCR3$^+$ and other B cells ($P < 2 \times 10^{-16}$). **l**, Heatmap of differential expression levels of chemotaxis genes between T-bet$^+$CXCR3$^+$ and other B cells with significance (*$P < 0.5$). Significant adjusted P values displayed: 2.26×10^{-167} for CXCR3, 4.56×10^{-32} for CCL5, 2.35×10^{-37} for CCR7 and 3.80×10^{-3} for CCL3. P values for differential gene expression analysis between groups were calculated using the two-sided MWU test. Panels **j**,**l** were adjusted for multiple comparisons using the Benjamini–Hochberg correction. *$P < 0.05$ and ****$P < 0.0001$.

Our analysis revealed significantly increased levels of *ALCAM* and *LFA1* in T-bet$^+$CXCR3$^+$ B cells (Fig. 3j). In addition, T-bet$^+$CXCR3$^+$ cells displayed significantly higher levels of chemotaxis genes such as *CXCR3*, *CCL5* and *CCL3* (Fig. 3k,l). Our findings are supported by a previous study that also found *CCL3* and *CCL5* to be upregulated during de novo EBV infection of ABCs and in the B cells of a patient diagnosed with clinically isolated syndrome[25]. Thus, EBV seems to infect T-bet$^+$CXCR3$^+$ B cells, allowing them to oligoclonally expand and acquire CNS homing capacity.

To investigate whether EBV-infected oligoclonally expanded B cells home to the CNS, we performed scRNA-seq on matched CD19$^+$ B cells from the perfused brain and spleen of ten EBV-infected and three PBS mock-infected humanized BRGS-A2DR2 mice, 6 weeks post-infection. We re-identified five B cell clusters in EBV-infected mice and visualized them on *t*-distributed stochastic neighbour embedding (tSNE) plots for the brain and spleen (Extended Data Fig. 5a). Brain-derived B cells were enriched for memory and plasma cells (Extended Data Fig. 6a). EBV transcripts were primarily detected in cycling B cells and, to a lesser extent, in memory and plasma cells (Extended Data Fig. 6b), and were associated with the strongest clonal B cell expansion in both the spleen and the brain (Extended Data Fig. 5b). EBV-driven oligoclonal expansion was more prominent in B cells from the brain than the spleen (Extended Data Fig. 6c). PBS mice lacked the CNS-infiltrating non-naive B cell clusters in both the spleen and the brain, as well as oligoclonally expanded B cells in the CNS (Extended Data Fig. 6d,e). Multiple B cell clones with distinct BCRs were shared between the brain and spleen in EBV-infected mice (Extended Data Fig. 5c). In one PBS mouse, clonal sharing between the spleen and brain B cells was also observed, but at much lower clonal cell counts than EBV-infected mice (Extended Data Fig. 6f). Differential gene expression analysis revealed that CD137L (also known as 4-1BBL or TNFSF9) expression was enriched in brain-derived versus spleen-derived memory B cells (Extended Data Fig. 6g). TNFSF9 is essential for EBV-specific immune control, as patients with deficiencies in this gene are highly susceptible to EBV-associated malignancies[26]. Furthermore, we detected enrichments for certain immunoglobulin heavy chain variable regions (IGHVs) among oligoclonally expanded B cells that were further enriched in the brain of EBV-infected mice (Extended Data Fig. 6h). These included IGHV4-34-carrying and IGHV4-39-carrying clones (Extended Data Fig. 4l). In fact, these IGHV segments were found on more than half of the expanded B cell clones (28 of 51) in one of our two scRNA-seq experiments, including the three most expanded clones. These two IGHVs have previously been described to

be enriched in oligoclonal B cells that were recovered from brain lesions of patients with MS[27]. Thus, oligoclonal B cells expanded by direct EBV infection preferentially home to the brain and some of them carry BCRs with similar IGHV usage as oligoclonal B cell expansions found in the CNS of patients with MS.

To shed more light on the specificity of these oligoclonal B cell expansions, which were preferentially IgM (Extended Data Fig. 4c) and shared between plasma cells and memory B cells (Extended Data Fig. 4f), we performed IgM ELISAs using blood plasma from the ten EBV-infected humanized BRGS-A2-DR2 mice used for scRNA-seq of brain and splenic B cell compartments. For this purpose, membranes were spotted with recombinant proteins covering all EBV gene products and tested for IgM antibody recognition (Extended Data Fig. 5d). Compared with the three PBS controls (mice 1, 6 and 10), which showed no reactivity, all EBV-infected mice recognized some EBV proteins without any clear immunodominance of particular EBV proteins. Combined with a previous experiment, in which three pools, each containing plasma from two to three EBV-infected (pools 1–3), or PBS control mice (pool 4) were used (Extended Data Fig. 6j). BXLF2 (gH) and LMP2A were the most consistent antibody targets. In parallel, the same blood plasma samples were also incubated with a membrane spotted with common autoantigens (Extended Data Fig. 6i). Half of the EBV-infected mice produced IgM that bound to autoantigens. ADRB1 and RBM33 were the most frequently recognized targets (Extended Data Fig. 6i) and have previously been implicated in regulating microglia function during senescence and inflammation[28,29]. Thus, the oligoclonal memory B and plasma cell expansions carrying IgM BCRs seem to frequently recognize EBV antigens and possibly also CNS-associated autoantigens.

Brain homing LCLs attract T cells

To determine whether T-bet$^+$CXCR3$^+$ B cells can independently migrate to the CNS or simply follow other lymphocytes crossing the blood–brain barrier, we intravenously transferred T-bet and CXCR3-expressing EBV-Luc-transformed LCLs into non-reconstituted BRGS-A2DR2 mice (Fig. 4a). We tested cell lines from two different healthy donors and one LCL generated from splenocytes of humanized BRGS-A2DR2 mice. T-bet expression in the tested LCLs ranged from 6.1% to 16.9% and CXCR3 expression from 6.0% to 25.7% before transfer (Extended Data Fig. 7a,b). All three cell lines demonstrated the ability to migrate into mouse brains in the absence of any other lymphocytes, with infiltration occurring in over 90% of mice across all experiments (Fig. 4b–d and Extended Data Fig. 7c). CNS-infiltrating B cells predominantly localized to submeningeal areas and, to a lesser extent, perivascular sites in the parenchyma (Extended Data Fig. 7d–g). This is in line with findings from patients with MS, where B cells are primarily found below the meninges[24,30,31]. Although T-bet expression was higher in the cells that migrated to the brain than those migrating to the spleen, a large proportion on T-bet$^-$ LCLs were also able to infiltrate the CNS. It remains unclear whether these cells downregulate T-bet upon tissue entry, or whether neuroinvasion is not strictly dependent on T-bet expression (Fig. 4e). To better understand the involvement of T-bet and CXCR3 in neuroinvasion, we decided to study the expression of these markers independently of each other. To that end, T-bet^{high} and T-bet^{low} LCLs, which showed similar levels of CXCR3 expression (Extended Data Fig. 7h), were intravenously injected into non-reconstituted BRGS-A2DR2 mice. Analysis of EBV viral load of the CNS revealed that T-bet^{low} and T-bet^{high} LCLs with similar CXCR3 expression migrated similarly into the CNS (Extended Data Fig. 7l). In addition, a positive correlation was observed between CXCR3 expression on B cells in the blood and CNS infiltration, but no correlation was observed between T-bet expression and CNS infiltration (Extended Data Fig. 7i,j). To test whether CXCR3 is indeed responsible for CNS migration, we injected T-bet-expressing CXCR3^{high} LCLs intravenously into mice and treated them with a CXCR3 and CCR5 antagonist (TAK-779). As CCR5 is not expressed on LCLs[32], this treatment specifically blocked CXCR3 in these LCL transfer experiments. We indeed found that mice receiving the CXCR3 antagonist (CXCR3^{block}) showed a strong reduction in CNS migration by LCL compared with untreated mice (CXCR3^{high}; Extended Data Fig. 7m). Splenic EBV infection correlated with CNS infiltration in untreated but not CXCR3 antagonist-treated mice, indicating that inhibition of CXCR3 specifically prevented LCLs from homing to the CNS without affecting their ability to home to the spleen (Fig. 4f,g). Natalizumab, a treatment frequently used in patients with MS, also efficiently reduced LCL migration to the CNS in our in vivo model (Extended Data Fig. 7n). These results are in line with similar findings in patients with MS, where CXCR3$^+$ B cells preferentially infiltrate the CNS[23]. This indicates that CXCR3 expression is primarily responsible for neuroinvasion. To determine whether LCLs migrating to the CNS can attract T cells, we performed in vitro transwell migration assays using supernatants from LCLs. This revealed that LCL supernatants promoted migration of activated CD4$^+$ T cells and, to a lesser extent, CD8$^+$ T cells (Fig. 4h,i and Extended Data Fig. 7o,p). The supernatants of the LCLs contained chemokines such as CCL3, CCL4, CCL5, CXCL9, CXCL10 and the pro-inflammatory cytokine TNF (Fig. 4j). To assess which one of these chemokines are crucial for recruiting T cells, the supernatant was either treated with neutralizing antibodies to CCL3, CCL4 and CCL5 or with a CXCR3 and CCR5 antagonist (TAK-779). Neutralization of CCL3, CCL4 and CCL5 led to a small reduction in CD4$^+$ and a significant reduction in CD8$^+$ T cell recruitment. CXCR3 and CCR5 antagonist treatment led to a significant reduction in both CD4$^+$ and CD8$^+$ T cell migration (Fig. 4k and Extended Data Fig. 7q). To further confirm that CXCL9 and CXCL10 are potential key drivers of T cell recruitment and are upregulated following EBV infection, we generated LCLs with either wild-type B95-8 EBV or *EBNA3B*-deficient (knockout) B95-8 EBV. EBNA3B is known to enhance the production of the chemokines CXCL9 and CXCL10 (refs. 33,34). Indeed, we found that supernatant from *EBNA3B*-knockout LCLs recruited fewer T cells and contained less CXCL9 and CXCL10 (Extended Data Fig. 7r,s). To see whether T cell attraction is also more pronounced in T-bet-expressing LCLs, supernatant from T-bet^{high} and T-bet^{low} LCLs were used in T cell migration assays. A significant reduction in the CD4$^+$ but not in CD8$^+$ T cell migration could be observed (Fig. 4l and Extended Data Fig. 7t). Together, these findings suggest that EBV-infected T-bet$^+$CXCR3$^+$ B cells preferentially home to the submeningeal CNS areas, a process that primarily relies on CXCR3 expression. Furthermore, they have the capacity to recruit activated T cells through EBNA3B-dependent production of CXCL9. Other chemokines, such as CCL3, CCL4 and CCL5, act synergistically to further enhance T cell recruitment.

B cell depletion inhibits neuroinvasion

To assess whether depletion of B cells during EBV infection would diminish T cell infiltration into the brain, we administered rituximab to a subset of EBV-infected mice starting 2 weeks post-infection (Fig. 5a). Treatment with rituximab significantly diminished the frequency and total numbers of CD20$^+$ and, to a lesser extent, CD19$^+$ B cells in the blood, spleen and brain (Fig. 5b–d and Extended Data Fig. 8a–f). Although CD20$^+$ B cells were depleted in rituximab-treated mice, viral loads persisted in some mice, possibly in CD19$^+$CD20$^-$ B cell reservoirs. However, their numbers were significantly lower and were undetectable in the spleen and brain of more than half of the treated mice (Fig. 5e–g). This reduction was further confirmed by in vivo imaging of perfused brains, showing decreased EBV infection in brains of rituximab-treated mice (Extended Data Fig. 8g). In addition, rituximab treatment eliminated T-bet$^+$CXCR3$^+$ B cells in the blood, spleen and brain (Fig. 5h–j and Extended Data Fig. 8h). Analysis of T lymphocyte infiltration revealed a positive correlation between total CD19$^+$T-bet$^+$CXCR3$^+$ B

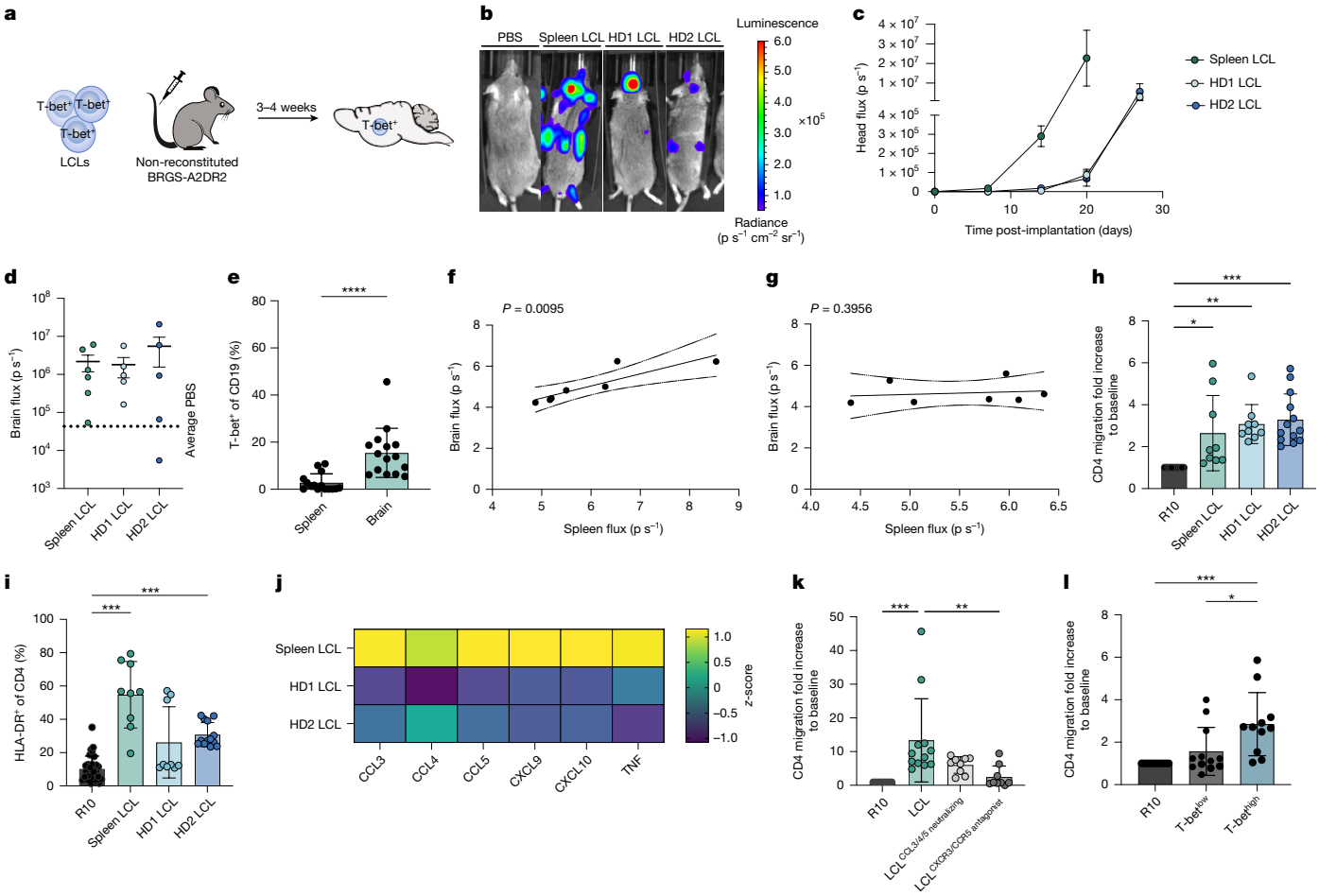

Fig. 4 | EBV-infected B cells independently home to the brain and attract T cells. a, Schematic of the experimental approach. **b**,**c**, Representative image of the bioluminescence signal in mice (**b**) and quantification of the signal intensity over time from the head area (**c**). Each dot represents one experiment ($n = 8$ for spleen LCLs, $n = 7$ for HD1 LCLs and $n = 5$ for HD2 LCLs). **d**, Bioluminescence intensity measured from the perfused brain ($n = 6$ for spleen LCLs, $n = 5$ for HD1 LCLs and $n = 5$ for HD2 LCLs). **e**, Frequency of T-bet$^+$CD19$^+$ B cells in the spleen and brain ($P < 0.001$). Each dot represents one mouse ($n = 15$ for the spleen and $n = 15$ for the brain). The P value was obtained using the two-sided MWU test. **f**,**g**, Correlation between viral loads measured by EBV-encoded luciferase activity by in vivo imaging in the brain and spleen without (**f**) and with (**g**) CXCR3 inhibition. The solid line represents the trend obtained from linear regression, and the dotted lines indicate 95% confidence bands ($n = 7$). A two-tailed P value was calculated using Spearman correlation. **h**, Transwell migration assays with supernatant from LCLs from the spleen ($P = 0.0424$), HD1 ($P = 0.0041$) and HD2 ($P = 0.0006$). **i**, Frequency of HLA-DR$^+$CD4$^+$ T cells among migrated cells ($P = 0.0001$ for spleen LCLs and $P = 0.0008$ for HD2 LCLs). **j**, z-scored heatmap displaying normalized expression of cytokines. **k**, Transwell migration assays with supernatant from LCLs ($P = 0.0003$) with CCL3, CCL4 and CCL5 neutralizing antibodies or a CXCR3 and CCR5 antagonist (TAK-779; $P = 0.0028$). **l**, Transwell migration assays with supernatant of T-bet^{high} ($P = 0.0004$) or T-bet^{low} ($P = 0.0128$) LCLs from the same donors. R10 indicates medium alone. Each dot represents one well. The P values in panels **h**,**i**,**k**,**l** were calculated using one-way analysis of variance with Dunnett's multiple comparison test. Data from panels **c**–**e** were generated from three independent experiments. Data from panels **f**,**g** were generated from two independent experiments with two LCL donors. Each condition and donors in the migration assays were tested with at least three T cell donors (**h**,**i** and **k**,**l**, respectively). $^*P < 0.05$, $^{**}P < 0.01$, $^{***}P < 0.001$ and $^{****}P < 0.0001$. Error bars indicate s.e.m.

cells in the brain and CNS infiltration of CD8$^+$ T cells (Fig. 5k). Treatment of EBV-infected mice with rituximab diminished the total numbers of CD8$^+$ T cells, activated CD8$^+$HLA-DR$^+$, activated CD4$^+$HLA-DR$^+$ and CD8$^+$PD1$^+$ T cells in the CNS (Fig. 5m–o). Although there was no difference in the total numbers of naive CD8$^+$ T cells between EBV-infected and rituximab-treated animals, a significant decrease in effector and central memory CD8$^+$ T cell populations was observed in the brains of treated mice (Fig. 5p). Thus, lymphocyte populations show reduced CNS trafficking in the absence of T-bet$^+$CXCR3$^+$ B cells. Although there was no difference in the memory population or total numbers of CD4$^+$ T cells in the brains upon rituximab treatment, we observed a significant decrease of CD4$^+$ T cell activation. Furthermore, there was a positive correlation between the total number of activated HLA-DR$^+$CD4$^+$ T cells and CD19$^+$T-bet$^+$CXCR3$^+$ B cells in the brain (Extended Data Fig. 8i–k). Together, our findings suggest that T-bet$^+$CXCR3$^+$ B cells are required to recruit activated T cells to the brain during primary EBV infection. This T cell infiltration, particularly by activated CD4$^+$ T cells that correlate with NfL release as a sign of neuroaxonal damage, might initiate the prodromal phase of MS.

Discussion

In our humanized mouse model of infectious mononucleosis-like primary infection, EBV expands oligoclonal and CNS-homing B cell populations, which might act as trailblazers, attracting lymphocytes, including both activated CD4$^+$ and CD8$^+$ T cells, to infiltrate brains and initiate MS.

Although we observed EBV transcripts in BCR clonally related T-bet$^-$CXCR3$^-$ circulating B cells, the minority of T-bet$^+$CXCR3$^+$ CNS-homing memory B cells had detectable EBV transcripts. This could

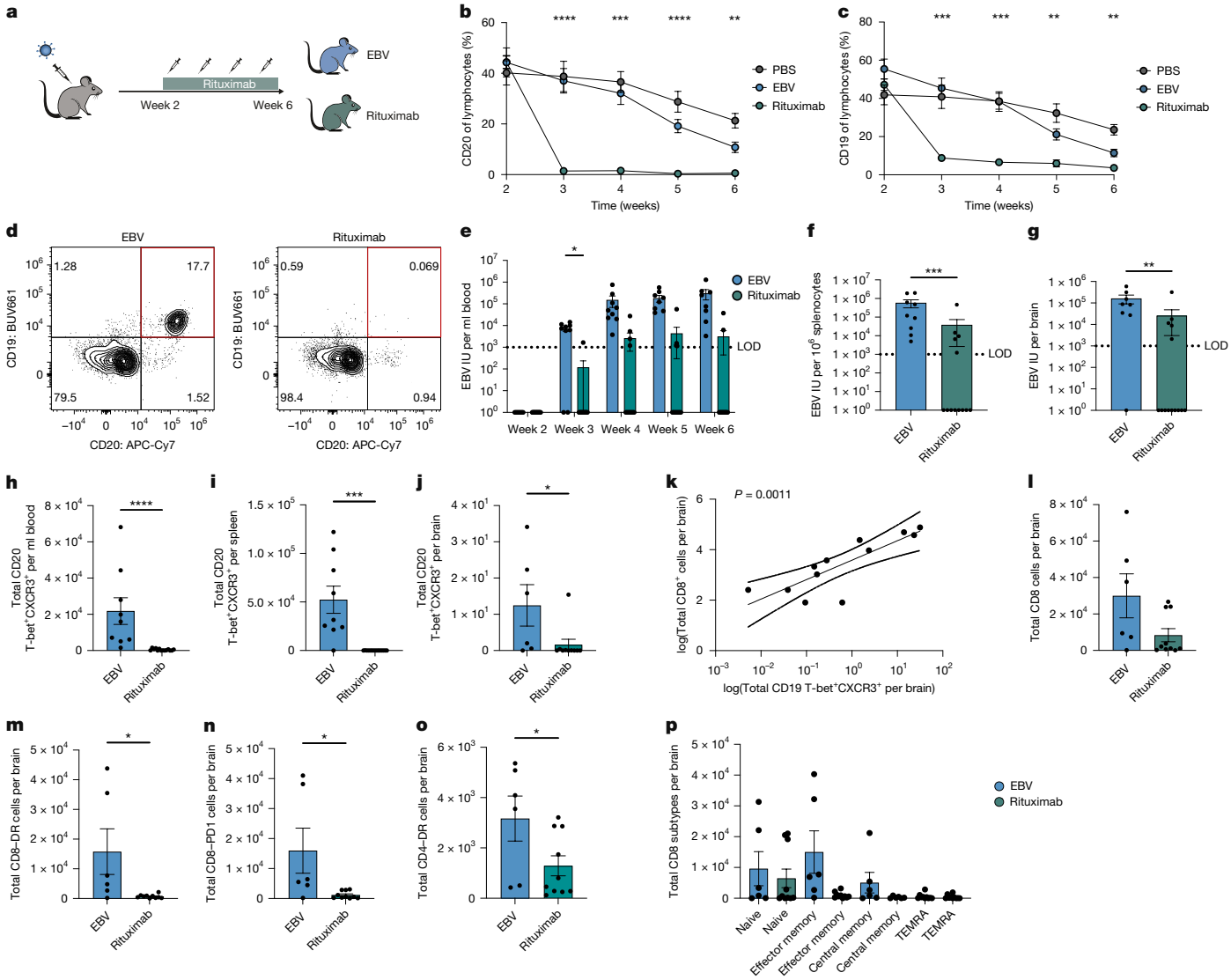

Fig. 5 | Depletion of B cells during EBV infection diminishes T cell infiltrates in the brain. a, Schematic of the experimental approach. **b**,**c**, Percentage of CD20$^+$ (**b**; *P* values from left to right: less than 0.0001, 0.0001, less than 0.0001 and 0.0016) and CD45$^+$CD19$^+$ (**c**; *P* values from left to right: 0.0002, 0.0006, 0.0015 and 0.0095) B cells in weekly blood draws comparing EBV-infected mice to rituximab-treated mice ($n = 7$ for PBS, $n = 9$ for EBV and $n = 14$ for rituximab). A two-way mixed-effects model with Geisser–Greenhouse correction followed by Tukey's multiple comparisons test was used. **d**, Representative flow cytometry plot, gated on single, live, CD45$^+$, CD19$^+$ and CD20$^+$ cells. The *P* value was calculated using a mixed-effects model with Geisser–Greenhouse correction followed by Sidak's multiple comparisons test. **e**–**g**, IU of EBV per millilitre blood (**e**; $P = 0.012$), 10^6 splenocytes (**f**; $P = 0.0003$) or per brain (**g**; $P = 0.0005$) in EBV-infected or rituximab-treated mice ($n = 8$ for EBV and $n = 14$ for rituximab). LOD, limit of detection. **h**–**j**, Total numbers of CD20$^+$T-bet$^+$CXCR3$^+$ B cells from the blood (**h**; $P < 0.0001$; $n = 9$ for EBV and $n = 14$ for rituximab), spleen (**i**; $P = 0.0002$; $n = 9$ for EBV and $n = 14$ for rituximab) and brain (**j**; $P = 0.0201$; $n = 6$ for EBV and $n = 10$ for rituximab) of EBV-infected or rituximab-treated mice. **k**, Correlation between the total number CD8$^+$ T cells and the total number of CD19$^+$T-bet$^+$CXCR3$^+$ B cells in the brain. **l**–**o**, Total numbers of CD8$^+$ (**l**), CD8$^+$HLA-DR$^+$ (**m**; $P = 0.0160$), CD8$^+$PD1$^+$ (**n**; $P = 0.0160$) and CD4$^+$HLA-DR$^+$ (**o**; $P = 0.0420$) T cells in the brains of EBV-infected or rituximab-treated mice ($n = 6$ for EBV and $n = 10$ for rituximab). **p**, Total numbers of CD8$^+$ T cell differentiation subtypes, naive (CD45RA$^+$CCR7$^+$), effector memory (CD45RA$^-$CCR7$^-$), central memory (CD45RA$^-$CCR7$^+$) and TEMRA (CD45RA$^+$CCR7$^-$) cells in EBV-infected or rituximab-treated mice ($n = 6$ for EBV and $n = 10$ for rituximab). Panels **b**–**p** were generated from two independent experiments with mice reconstituted from two human CD34$^+$ HPC donors. The *P* values in panels **f**–**j**,**l**–**o** were calculated using a two-tailed MWU test. In panel **k**, the solid line represents a trend line obtained by linear regression, and the dotted lines indicate 95% confidence bands; the two-tailed *P* value was calculated using Spearman correlation. The error bar indicates s.e.m. Each dot represents one single mouse. *$P < 0.05$, **$P < 0.01$, ***$P < 0.001$ and ****$P < 0.0001$.

suggest that T-bet$^+$CXCR3$^+$ B cells carry reduced viral gene expression. Previously, EBV has been shown to express all six EBNAs and the two LMPs in naive B cells of healthy virus carriers[35]. This expression program, known as latency III, is also found in LCLs[36]. However, upon transition to memory B cells, most viral gene expression is shut down, with only EBNA1 being expressed in homeostatically proliferating memory B cells, a state that is termed latency I program[37]. These memory B cells can differentiate into plasma cells, and differentiation-associated lytic EBV replication can be initiated from latency I Burkitt lymphoma cells upon BCR crosslinking[38]. Accordingly, T-bet$^+$CXCR3$^+$ B cells constitute a small cellular subset of LCLs that might be precursors of lytic EBV replication supporting plasmablasts[36], and T-bet$^+$ B cells from post-mortem MS brains support plasma cell differentiation[23]. A reservoir of EBNA1-expressing T-bet$^+$CXCR3$^+$ B cells might also explain why primarily EBNA1-specific antibodies and T cell populations are elevated in patients with MS[5,39–41].

Another feature of the CNS-homing B cells that we observed during EBV infection of humanized mice was their oligoclonal BCR expression.

This is reminiscent of the oligoclonal bands of antibody specificities found in the cerebrospinal fluid of patients with MS[1]. Indeed, these bands might originate from plasma cells that differentiate from oligoclonal T-bet$^+$CXCR3$^+$ B cells in the CNS. Some of these oligoclonal antibodies cross-react to EBNA1 and CNS autoantigens, such as GlialCAM, anoctamin 2 and α-crystallin B, often targeting intracellular epitopes of these antigens[8,42,43]. Therefore, these antibodies could reflect the BCR repertoires of T-bet$^+$CXCR3$^+$ B cells from which the respective plasma cells have differentiated. Such cross-reactive BCRs could facilitate antigen uptake and presentation to inflammatory T cell populations in the CNS during MS development. Therefore, it is tempting to speculate that MS arising from EBV infection is due to a rare event in which EBV infects autoreactive B cells, endowing them with the capacity to home to the CNS and to attract and stimulate T cells. Targeting this B cell population could modify MS pathology and needs further investigation to reveal its potential benefits for patients.

Online content

Any methods, additional references, Nature Portfolio reporting summaries, source data, extended data, supplementary information, acknowledgements, peer review information; details of author contributions and competing interests; and statements of data and code availability are available at https://doi.org/10.1038/s41586-025-09378-0.

1. Bjornevik, K. et al. Longitudinal analysis reveals high prevalence of Epstein–Barr virus associated with multiple sclerosis. *Science* **375**, 296–301 (2022).
2. Filippi, M. et al. Multiple sclerosis. *Nat. Rev. Dis. Primers* **4**, 43 (2018).
3. Oksenberg, J. R., Baranzini, S. E., Sawcer, S. & Hauser, S. L. The genetics of multiple sclerosis: SNPs to pathways to pathogenesis. *Nat. Rev. Genet.* **9**, 516–526 (2008).
4. Bray, P. F., Bloomer, L. C., Salmon, V. C., Bagley, M. H. & Larsen, P. D. Epstein–Barr virus infection and antibody synthesis in patients with multiple sclerosis. *Arch. Neurol.* **40**, 406–408 (1983).
5. Leibowitz, U. et al. Epidemiological study of multiple sclerosis in Israel. II. Multiple sclerosis and level of sanitation. *J. Neurol. Neurosurg. Psychiatry* **29**, 60–68 (1966).
6. Angelini, D. F. et al. Increased CD8$^+$ T cell response to Epstein–Barr virus lytic antigens in the active phase of multiple sclerosis. *PLoS Pathog.* **9**, e1003220 (2013).
7. Lünemann, J. D. et al. Increased frequency and broadened specificity of latent EBV nuclear antigen-1-specific T cells in multiple sclerosis. *Brain* **129**, 1493–1506 (2006).
8. Lanz, T. V. et al. Clonally expanded B cells in multiple sclerosis bind EBV EBNA1 and GlialCAM. *Nature* **603**, 321–327 (2022).
9. Bar-Or, A. et al. Rituximab in relapsing-remitting multiple sclerosis: a 72-week, open-label, phase I trial. *Ann. Neurol.* **63**, 395–400 (2008).
10. Hauser, S. L. et al. B-cell depletion with rituximab in relapsing-remitting multiple sclerosis. *N. Engl. J. Med.* **358**, 676–688 (2008).
11. Hauser, S. L. et al. Ocrelizumab versus interferon β-1a in relapsing multiple sclerosis. *N. Engl. J. Med.* **376**, 221–234 (2017).
12. Rubtsova, K. et al. B cells expressing the transcription factor T-bet drive lupus-like autoimmunity. *J. Clin. Invest.* **127**, 1392–1404 (2017).
13. Punnanitinont, A. et al. TLR7 activation of age-associated B cells mediates disease in a mouse model of primary Sjogren's disease. *J. Leukoc. Biol.* **115**, 497–510 (2024).
14. Tsubaki, T. et al. Accumulation of plasma cells expressing CXCR3 in the synovial sublining regions of early rheumatoid arthritis in association with production of Mig/CXCL9 by synovial fibroblasts. *Clin. Exp. Immunol.* **141**, 363–371 (2005).
15. Fox, R. I., Luppi, M., Kang, H. I. & Pisa, P. Reactivation of Epstein–Barr virus in Sjogren's syndrome. *Springer Semin. Immunopathol.* **13**, 217–231 (1991).
16. James, J. A. et al. Systemic lupus erythematosus in adults is associated with previous Epstein–Barr virus exposure. *Arthritis Rheum.* **44**, 1122–1126 (2001).
17. Alspaugh, M. A., Jensen, F. C., Rabin, H. & Tan, E. M. Lymphocytes transformed by Epstein–Barr virus. Induction of nuclear antigen reactive with antibody in rheumatoid arthritis. *J. Exp. Med.* **147**, 1018–1027 (1978).
18. SoRelle, E. D. et al. Time-resolved transcriptomes reveal diverse B cell fate trajectories in the early response to Epstein–Barr virus infection. *Cell Rep.* **40**, 111286 (2022).
19. Mouat, I. C. et al. Gammaherpesvirus infection drives age-associated B cells toward pathogenicity in EAE and MS. *Sci. Adv.* **8**, eade6844 (2022).
20. Miller, G. & Lipman, M. Comparison of the yield of infectious virus from clones of human and simian lymphoblastoid lines transformed by Epstein–Barr virus. *J. Exp. Med.* **138**, 1398–1412 (1973).
21. Miller, G. & Lipman, M. Release of infectious Epstein–Barr virus by transformed marmoset leukocytes. *Proc. Natl Acad. Sci. USA* **70**, 190–194 (1973).
22. Zdimerova, H. et al. Attenuated immune control of Epstein–Barr virus in humanized mice is associated with the multiple sclerosis risk factor HLA-DR15. *Eur. J. Immunol.* **51**, 64–75 (2021).
23. van Langelaar, J. et al. Induction of brain-infiltrating T-bet-expressing B cells in multiple sclerosis. *Ann. Neurol.* **86**, 264–278 (2019).
24. Jain, R. W. & Yong, V. W. B cells in central nervous system disease: diversity, locations and pathophysiology. *Nat. Rev. Immunol.* **22**, 513–524 (2022).
25. SoRelle, E. D. et al. An EBV-associated atypical B cell signature in clinically isolated syndrome is implicated in progression of multiple sclerosis. Preprint at *medRxiv* https://doi.org/10.1101/2023.02.26.23286433 (2024).
26. Fournier, B. et al. Inherited TNFSF9 deficiency causes broad Epstein–Barr virus infection with EBV$^+$ smooth muscle tumors. *J. Exp. Med.* **219**, e20211682 (2022).
27. Baranzini, S. E. et al. B cell repertoire diversity and clonal expansion in multiple sclerosis brain lesions. *J. Immunol.* **163**, 5133–5144 (1999).
28. Yang, X. et al. Liquid–liquid phase separation of RBM33 facilitates hippocampus aging by inducing microglial senescence by activating CDKN1A. *Int. J. Biol. Macromol.* **310**, 142986 (2025).
29. Evans, A. K. et al. Impact of noradrenergic inhibition on neuroinflammation and pathophysiology in mouse models of Alzheimer's disease. *J. Neuroinflammation* **21**, 322 (2024).
30. Reali, C. et al. B cell rich meningeal inflammation associates with increased spinal cord pathology in multiple sclerosis. *Brain Pathol.* **30**, 779–793 (2020).
31. Choi, S. R. et al. Meningeal inflammation plays a role in the pathology of primary progressive multiple sclerosis. *Brain* **135**, 2925–2937 (2012).
32. McHugh, D. et al. EBV renders B cells susceptible to HIV-1 in humanized mice. *Life Sci. Alliance* **3**, e202000640 (2020).
33. White, R. E. et al. EBNA3B-deficient EBV promotes B cell lymphomagenesis in humanized mice and is found in human tumors. *J. Clin. Invest.* **122**, 1487–1502 (2012).
34. Münz, C. Latency and lytic replication in the oncogenesis of the Epstein Barr virus. *Nat. Rev. Microbiol.* **17**, 691–700 (2019).
35. Babcock, J. G., Hochberg, D. & Thorley-Lawson, A. D. The expression pattern of Epstein–Barr virus latent genes in vivo is dependent upon the differentiation stage of the infected B cell. *Immunity* **13**, 497–506 (2000).
36. SoRelle, E. D., Reinoso-Vizcaino, N. M., Horn, G. Q. & Luftig, M. A. Epstein–Barr virus perpetuates B cell germinal center dynamics and generation of autoimmune-associated phenotypes in vitro. *Front. Immunol.* **13**, 1001145 (2022).
37. Hochberg, D. et al. Demonstration of the Burkitt's lymphoma Epstein–Barr virus phenotype in dividing latently infected memory cells in vivo. *Proc. Natl Acad. Sci. USA* **101**, 239–244 (2004).
38. Nowag, H. et al. Macroautopphagy proteins assist Epstein Barr virus production and get incorporated into the virus particles. *EBioMedicine* **1**, 116–125 (2014).
39. Lünemann, J. D. et al. EBNA1-specific T cells from patients with multiple sclerosis cross react with myelin antigens and co-produce IFN-γ and IL-2. *J. Exp. Med.* **205**, 1763–1773 (2008).
40. Serafini, B., Rosicarelli, B., Veroni, C., Mazzola, G. A. & Aloisi, F. Epstein–Barr virus-specific CD8 T cells selectively infiltrate the brain in multiple sclerosis and interact locally with virus-infected cells: clue for a virus-driven immunopathological mechanism. *J. Virol.* https://doi.org/10.1128/JVI.00980-19 (2019).
41. Gottlieb, A., Pham, H. P. T., Saltarrelli, J. G. & Lindsey, J. W. Expanded T lymphocytes in the cerebrospinal fluid of multiple sclerosis patients are specific for Epstein–Barr-virus-infected B cells. *Proc. Natl Acad. Sci. USA* **121**, e2315857121 (2024).
42. Thomas, O. G. et al. Cross-reactive EBNA1 immunity targets α-crystallin B and is associated with multiple sclerosis. *Sci. Adv.* **9**, eadg3032 (2023).
43. Tengvall, K. et al. Molecular mimicry between anoctamin 2 and Epstein–Barr virus nuclear antigen 1 associates with multiple sclerosis risk. *Proc. Natl Acad. Sci. USA* **116**, 16955–16960 (2019).

Methods

Animal and viral infection model

BRGS-A2DR2 (provided by Regeneron) or NSG were maintained under specific pathogen-free conditions at the laboratory animal service center at the University of Zürich, Switzerland. Newborn pups (1–5 days of age) were sublethally irradiated with 3 Gy (BRGS-A2DR2) or 1 Gy (NSG); 5 h later, intrahepatical injection with around 2×10^5 HLA-DRB1*1501$^+$ human fetal liver-derived (Advanced Bioscience Resources) CD34$^+$ HPCs was performed. CD34$^+$ HPCs were isolated by magnetic bead separation based on the manufacturer's instructions (Miltenyi Biotech). Both female and male mice 3–6 months of age and engrafted with human immune cells were intraperitoneally injected with 10^5 luciferase-expressing EBV (B95-8) Raji infectious units (RIU) or PBS and monitored for 5–6 weeks. Male and female mice aged 2–8 months were used for the experiments. Humanized mice were block-randomized into experimental groups based on sex and the frequency of reconstituted human immune cells in peripheral blood before EBV infection, ensuring comparable sex ratios and similar levels of immune reconstitution across groups. Blinding was not feasible for in vivo experiments, as the same researcher conducted the planning, execution and monitoring of all mouse procedures, including infection and treatment. Sample sizes were determined on the basis of previous experience with comparable in vivo models. For CD20 depletion, animals were injected with rituximab (Mab Thera, Roche) once a week at a concentration of 10 mg kg^{-1} intraperitoneally (i.p.) starting 2 weeks post-infection. EBV-injected mice were excluded from the dataset if they failed to show blood viral loads during the experiments. Rituximab-treated mice were excluded from the dataset if their B cell counts after depletion were within or above the range of the mean + s.e.m. of the EBV-infected control group. Post-euthanasia and before brain collection, all mice were transcardiac perfused using PBS solution. All procedures were strictly performed in accordance with the animal protocols ZH 212/20 and ZH189/23, licensed by the veterinary office of the canton of Zürich, Switzerland.

EBV

Luciferase-encoding EBV B95-8 (EBV-Luc) producer cells were provided by W. Hammerschmidt. The EBV-Luc genome was originally derived from the B95-8 EBV with bioluminescent firefly luciferase protein 58 incorporated as an EBV–EBNA2 fusion construct and produced in HEK293 cells. Virus concentrates were titrated on Raji cells (American Type Culture Collection) and GFP-expressing cells were analysed 2 days later by flow cytometry (FACSCanto II, BD Biosciences) to determine the EBV RIU.

In vivo bioluminescence imaging

Migration of EBV-infected cells either during primary EBV infection or after LCL transfer was measured by in vivo bioluminescence imaging with the IVIS Spectrum Imaging System (PerkinElmer). For measurement of the CNS bioluminescence after euthanasia, mice were i.p. injected with 150 mg kg^{-1} D-luciferin (Promega) and euthanized by carbon dioxide inhalation. Immediately afterwards, transcardiac perfusion with PBS was performed and CNS tissue was isolated. Bioluminescence was measured 15 min after the initial i.p. injection. For measurement of migration in live animals, mice were anaesthetized by isoflurane and injected i.p. with 150 mg kg^{-1} D-luciferin (Promega) 10 min before imaging. Mice were placed inside the IVIS imaging box and imaged dorsally. Representative images were acquired at 3 min for each mouse during the entire experiment to illustrate the virus progression within the host. Images were analysed with living image 4.3.1 software (PerkinElmer). Regions of interest (ROIs) were set to include the regions with luminescent signal in mice and photon flux (p s^{-1}) of light emitted per second within the ROI was measured as the readout.

Viral load quantification

CNS and splenic tissue were processed for DNA isolation using the DNeasy Blood and Tissue Kit (Qiagen), and total DNA from whole blood was extracted using the NucliSENS EasyMAG System (bioMérieux), following the manufacturer's instructions. TaqMan real-time PCR (Applied Biosystems) was used to quantify EBV DNA, with modified primers for the BamH1 W fragment (5′-CTTCTCAGTCCAGCGCGTTT-3′ and 5′-CAGTGGTCCCCCTCCCTAGA-3′) and a fluorogenic probe (5′-FAM-CGTAAGCCAGACAGCAGCCAATTGTCAG-TAMRA-3′). Samples were measured on an ABI Prism 7700 Sequence detector (Applied Biosystems) or on a C1000 Touch CFX384 Real-Time platform (Bio-Rad) and analysed in triplicates.

Flow cytometry analysis

For surface receptor staining, single-cell suspensions were incubated with specific antibodies in PBS at 4 °C for 20 min. For intranuclear staining, cells were fixed and permeabilized using the Foxp3/transcription factor staining buffer set (eBioscience) at room temperature for 30 min. Cells were then incubated with the required antibodies in a permeabilization buffer for 1 h at room temperature. The following antibodies were used in this study: CD45-BUV3955 (HI30, 1:100), CD4-BUV496 (SIK3, 1:50), CD8-BUV563 (RPA-T8 1:100), CD19-BUV661 (HIB19, 1:100), CD127-BUV805 (HIL-7R-M21, 1:100), CD27-BV421 (O323, 1:100), IgD-PB (IA6-3, 1:100), CD45RA-BV510 (HI100, 1:100), HLA-DR-BV605 (G46-6, 1:50), CD25-BV711 (2A3-1:50), CD3-BV785 (OKT-3, 1:100), PD1-FITC (EH12.2H7, 1:50), CD38-PerCP (HIT2, 1:50), CCR6-PE (11A9, 1:50), CCR7-PE-CF594 (G04H7, 1:50), CXCR3-PE Cy5 (1C6/CXCR3, 1:50), CCR4-PE Cy7 (1G1. 1:25), CCR10-APC (1B5, 1:25), CD21-BUV496 (B-ly4, 1:100), CD184-BUV563 (12G5, 1:100), FCRL4-BUV805 (A1, 1:100), CD38-BV711 (HIT2, 1:100), T-bet-PE (ebio4B10, 1:25), CD11c-PE Cy7 (B-ly6, 1:100), HLA-DR-APC (L243, 1:100), CD20-APC Cy7 (2H7, 1:100) and PE-IgG1 isotype (MOPC-21, 1:25). Cell viability was assessed using Fixable Viability dyes (Zombie Near-IR and Zombie Aqua, BioLegend).

Acquisition and compensation were performed on a Cytek Aurora spectral flow cytometer. Data were exported and analysed using FlowJo software (v10.9.4). Gating strategy was partially adapted from ref. 44. The gating strategy for T and B cell population is shown in Extended Data Fig. 9a–c. Graphs were generated using Prism (GraphPad Software). For UMAP generation of flow cytometric data, cells were manually gated on live, single human CD45$^+$CD3$^+$ T cells. Cells were analysed using the CRUSTY webtool (https://crusty.humanitas.it/)[45]. Clustering was performed using the FLOWSOM algorithm.

EBV infection of CXCR3^{high} and CXCR3^{low} B cells

Blood samples of healthy volunteers were collected under the cantonal ethics committee (KEK) approved protocol with the BASEC-Nr. 2019-00837 with informed consent. CD19$^+$ B cells were isolated from PBMCs of healthy donors using magnetic beads for CD19 (Miltenyi Biotec) according to the manufacturer's instruction. B cells were fluorescence-activated cell sorting (FACS) sorted (BD FACSAria III) into CXCR3$^+$ and CXCR3$^-$ populations. The sorting strategy for the experiment can be found in Extended Data Fig. 10b. A total of 5×10^5 CD19$^+$ cells per well were plated in a 96- well U-bottom plate in a total volume of 200 µl and cultured with EBV B95-8 with a multiplicity of infection of 0.5 in RPMI-1640 medium (Gibco) with 10% fetal bovine serum (Sigma), 1% L-glutamine (Gibco) and 1% penicillin–streptomycin (Gibco). Cells were maintained by incubation at 37 °C under a 5% CO_2 humidified atmosphere. Half of the medium was removed and replaced with fresh medium if supernatant turned yellow. Marker expression was assessed using flow cytometry. For growth analysis 1×10^6 cells were seeded of both CXCR3$^+$ and CXCR3$^-$ LCLs. Cells were counted on days 4 and 6 post-seeding to see difference in growth speed.

ChipCytometry

Splenic tissue was harvested at the end of the experiment, embedded in OCT medium (Tissue-Tek) and stored at −80 °C. The tissue was sectioned to a thickness of 6 µm using a Cryostat (Leica) where the chamber and the knife temperature was set to −18 °C and −15 °C, respectively. The samples were collected on 10% poly-L-lysine-coated formalin-fixed paraffin-embedded (FFPE) coverslips (Canopy) and fixed in 100% acetone for 5 min, followed by 90% ethanol and 70% ethanol for 3 min each. The samples were then washed twice in PBS for 5 min.

The FFPE chip was assembled, and the tissue was subsequently blocked for 1 h at room temperature in freshly prepared and filtered blocking buffer (10% normal mouse serum, 1% FCS and 0.1% Tween-20 in ROTI Cell PBS from Roth). Each staining cycle was preceded by a background scan in the relevant colour channel (or channels). After staining, unless stated otherwise, the chip was continuously washed for 5 min in PBS containing 0.1% Tween-20 using an automated Ismatec pump (2 rpm), followed by manual washing twice with 1 ml of PBS before the image was acquired. During acquisition, the chip was continuously washed with PBS using the automated Ismatec pump (0.2 rpm).

A 11-plex + Helix marker panel containing a total of eight staining cycles was applied to the tissue. The antibody master mix was prepared in freshly filtered blocking buffer and centrifuged at 16,000*g* at 4 °C for 10 min and was filtered before being added to the chip. All markers were stained at 4 °C unless stated otherwise.

Cycle 1 was stained for 60 min using the following antibody clones and dilutions: CD19-PE (SJ25C1, 1:10, and HIB19, 1:10). Cycle 2 was stained for 15 min using the following antibody clones and dilutions: CXCR3-PE (1C6/CXCR3, 1:20), CD8-PerCP (SK1, 1:30) and CD39-FITC (A1, 1:15). Cycle 3 was stained for 45 min using the following antibody clones and dilutions: CD4-PerCP (RPA-T4, 1:45), HLA-DR-FITC (G46.6, 1:120) and CD11c-PE (3.9, 1:400). Cycle 4 was stained for 30 min using the following antibody clone and dilution: CD20cyto-PerCP (1412, 1:20). Cycle 5 was stained for 15 min using the following antibody clone and dilution: CD45-BUV395 (HI30, 1:100). Cycle 6 was stained for 30 min using the following antibody clone and dilution: CD137-PE (4B4-1, 1:20).

Before staining the intranuclear T-bet, the tissue was permeabilized for 30 min using a 1× dilution of the Foxp3 permeabilization buffer (Thermo Fisher). An additional 1-h blocking cycle was conducted using blocking buffer made in 1× permeabilization buffer instead of PBS. All subsequent antibody master mixes were also made in this blocking buffer.

Cycle 7 was stained for 24 h using the following antibody clone and dilution: T-bet (QA18A24, 1:20). The chip was then washed with 1 ml of filtered and freshly prepared Foxp3 1× permeabilization buffer, followed by a continuous wash in PBS containing 0.1% Tween-20 for 20 min using the Ismatec pump (2 rpm), before it was manually washed twice with 1 ml of PBS. Cycle 8 was stained for 20 min using the nucleic acid stain Helix NP-FITC in a 1:400,000 dilution.

The dynamic compression and background factor were adjusted in the ZellExplorer App of the ChipCytometer before image export for each of the selected marker as follows: T-bet (10, 4), CD19 (26, 2), CD4 and CD8 (7, 2), HLA-DR (17, 2) and CXCR3 (3, 10).

ChipCytometry analysis

ChipCytometry images were shading corrected using Basic and stitched using ASHLAR. Stitched images were imported into QuPath and cells were segmented. Location, morphological phenotype and expression data were exported from each cell and imported into R. Cells were clustered using FlowSOM and annotated according to their canonical lineage marker expression. MetaCyto was used to assign positivity to functional markers per cell (for example, HLA-DR and Ki67, among others). Cellular neighbourhoods were determined as previously described. In brief, the phenotype of the immediate neighbours of each cell was determined and clustered using *k*-means. The microenvironment of cells of interest (for example, T-bet$^+$CXCR3$^+$ versus other B cells) was calculated using the nearest neighbour algorithm (RANN). Cell frequencies were then calculated from cells that resided within these microenvironments.

Tissue clearing

After transcardial perfusion with 4% paraformaldehyde in PBS, mouse brain hemispheres were extracted and fixed in a 4% paraformaldehyde in PBS solution for 2.5 h at 2–8 °C. For all of the following steps, brains were cut into hemispheres, kept at 24–28 °C, transferred to solutions in 50-ml tubes and kept protected from light. After fixation, the samples were washed in PBS and incubated in the permeabilization solution of the MACS Deep Clearing Kit (Miltenyi Biotec) for 24 h on a MACSmix Tube Rotator. Following this step, the 3D-IF antibodies anti-human CD3 VioG570 REAfinity (130-133-790), anti-human CD45 VioR667 REAfinity (130-128-742) and anti-mouse CD31 Vio780 REAfinity (130-135-521; all Miltenyi Biotec) were used for immunostaining. Antibodies were diluted in the antibody staining solution of the MACS Deep Clearing Kit, and the samples were incubated for 7 days at 28 °C with gentle shaking. After antibody incubation, the mouse brain hemispheres were washed with antibody staining solution and dehydrated in an ascending ethanol series in ddH_2O (v/v) at 30%, 50%, 70% and 100% (1.00986, Sigma-Aldrich) with 2% Tween-20 (v/v) (8.17072, Sigma-Aldrich) for at least 4 h while shaking. Finally, the mouse brain hemispheres were optically cleared by incubating them in the clearing solution of the MACS Deep Clearing Kit for at least 6 h at room temperature, under slow rotation on a MACSmix Tube Rotator.

Light-sheet fluorescence microscopy and image processing

Cleared brains were imaged using an Ultramicroscope Blaze and ImSpector (v7.8.1; both Miltenyi Biotec) equipped with a laser beam combiner (wavelengths of 405 nm, 488 nm, 561 nm, 639 nm and 785 nm), an sCMOS camera with a 2,048 × 2,048 pixel chip of 6.5-µm pixel size and three dipping objectives with magnification of ×1.1 (0.1 NA), ×4 (0.35 NA) and ×12 (0.53 NA), which could be combined with additional post-(de-)magnifications of ×0.6, ×1, ×1.66 or ×2.5. For image acquisition, cleared samples were mounted on the sagittal cutting plane on clamping slide holders (Miltenyi Biotec) and immersed in MACS Imaging Solution (Miltenyi Biotec) in the instrument's cuvette. The following band-pass emission filters (mean nanometres per spread) were used, depending on the excited fluorophores: 620/60 for VioG570, 680/30 for VioR667 and 805 long pass for Vio780.

The brains were imaged along the sagittal axis with the ×4 objective and ×1 post-magnification (overall ×4 magnification) with a 3-µm *z*-step size, 0.06 sheet NA (6.1-µm light-sheet thickness), 100% sheet width and using lightspeed mode and fast tiling scan. A mosaic was defined to cover the entirety of the brain and subsequently automatically subdivided into multiple single fields of view (FOVs) with 40 pixel overlap in *x* and *y* between the tiles. Both light-sheet sides were used (bilateral illumination). Laser power and exposure times were kept the same during measurements and were set to 80% power and 5-ms exposure time for VioG570, 70% power and 5-ms exposure time for VioR667 and 100% power and 20-ms exposure time for Vio780.

OME.TIF stacks (16 bit) were stitched and converted (MACS iQ View-3D Large Volume v1.3, Miltenyi Biotec) into Imaris files (.ims). 3D reconstruction and subsequent visualization was done using Imaris (v10.2; Oxford Instruments).

scRNA-seq

For scRNA-seq of CD19$^+$ B cells during EBV infection, humanized BRGS-A2DR2 mice were i.p. injected with 10^5 luciferase-encoding EBV (B95-8) RIU and monitored for 6 weeks. The spleens were collected, and single-cell isolation was performed. CD45$^+$CD19$^+$ B cells were FACS

sorted. In total, three samples were analysed; each sample consisted of cells pooled from three mice. The quality of the single-cell suspension was evaluated with a haemocytometer under a Leica DM IL LED Fluo microscope, and the quantity was assessed using an automated cell counter (LUNA-FX7, Logos). Approximately 20,000 cells per sample were loaded into the 10X Chromium controller. Library preparation followed the manufacturer's guidelines specified in the Chromium Next GEM Single Cell 5′ Reagent Kits User Guide (v2 Chemistry Dual Index). For sequencing, the resulting libraries were processed on an Illumina NovaSeq X platform with a 150-bp paired-end read configuration. An average depth of approximately 50,000 reads per cell was achieved during sequencing.

For the second scRNA-seq experiment, spleens and perfused brains were collected, single-cell isolation was performed and $CD45^+CD19^+$ B cells were FACS sorted. The sorting strategy for both scRNA-seq experiments can be found in Extended Data Fig. 10a. In total, the spleens and brains from 13 mice (10 for EBV and 3 for PBS) were multiplexed using hashtag oligonucleotides. Spleens and brains were then pooled separately. The quality of the single-cell suspension was evaluated with a haemocytometer under a Leica DM IL LED Fluo microscope, and the quantity was assessed using an automated cell counter (LUNA-FX7, Logos). The spleen and brain pooled samples were loaded into the 10X Chromium controller with approximately 30,000 cells per sample, respectively. Library preparation followed the manufacturer's guidelines specified in the Chromium Next GEM-X Single Cell 5′ Reagent Kits user guide. For sequencing, the resulting libraries were processed on an Illumina NovaSeq X platform with a 150-bp paired-end read configuration. An average depth of approximately 50,000 reads per cell was achieved during sequencing.

scRNA-seq analysis

For transcript alignment, the EBV genome, strain B95-8, was added to the reference human genome, GRCh38.p13 (release 42). Raw reads were processed with CellRanger (v7.2.0). scRNA-seq data processing and analysis were performed using R (v4.4.0) and the Seurat package (v5.1.0). Raw count matrices were processed using the standard Seurat workflow, including normalization, identification of highly variable features, scaling and dimensionality reduction. Principal component analysis was performed using the top 2,000 variable features. UMAP and tSNE were used for visualization, with the first 20 principal components used for the UMAP calculation and the first 30 principal components used for the tSNE calculation. Cell clusters were identified using FindNeighbors in Seurat and FindClusters functions. Clusters were named based on using label transfer with Seurat using the CellTypist Spleen reference (https://www.celltypist.org/organs), using the 'Curated_annotation' metadata.

Ig isotype was determined based on the expression of isotype-specific constant region genes. IgM-expressing cells were identified by IGHM expression, IgD by IGHD, IgG by IGHG1-4, IgA by IGHA1-2 and IgE by IGHE. TBX^+CXCR3^+ cells were identified by including only cells expressing both CXCR3 and TBX21 above a threshold of 0 (CXCR3 > 0 and TBX21 > 0). Cell-type annotation was refined using the Azimuth reference mapping tool (v0.5.0). BCR repertoire analysis was conducted using the scRepertoire package (v2.0.4). Clonal expansion was assessed based on BCR clonotype information. Differential gene expression analysis between groups was performed using the Wilcoxon rank sum test as implemented in Seurat. Gene set enrichment analysis was conducted using the UCell package (v2.8.0) to calculate module scores for specific gene signatures. Trajectory analysis was performed using the Slingshot package (v2.12.0). Cells were ordered in pseudotime, and genes differentially expressed along the trajectory were plotted using tradeSeq (v1.18.0). For visualization, ggplot2 (v3.5.1) and Seurat built-in functions were used to generate UMAP plots, feature plots, violin plots and heatmaps.

Multiplex dot-blot assay for measuring IgM responses

All annotated open reading frames of the prototypic EBV type 1 strain or fragments thereof, for example, BPFL1I-III (GenBank: V01555.2, M35547.1), the human IgM constant region (P01871), and over 100 known or putative autoantigens associated with multiple sclerosis and other autoimmune diseases were recombinantly expressed as C-terminal 6×histidine (His6)-tagged fusion proteins in HEK293T cells, as previously described[46]. After affinity purification using Ni-NTA agarose (Qiagen), protein integrity and size were confirmed by western blot with an anti-His6 mouse monoclonal IgG antibody[46]. Protein concentrations were estimated by Coomassie staining of polyacrylamide gels, comparing band intensities to bovine serum albumin standards and adjusted to approximately 10 μg ml^{-1}. To assess serum IgM antibody responses in humanized mice, a multiplex dot-blot assay was performed as previously described[47]. In brief, concentration-adjusted recombinant proteins were spotted on nitrocellulose membranes and incubated overnight at 4 °C with anti-His6 antibody (clone 3D5) and mouse serum diluted 1:250 or 1:1,000. Following washing, membranes were incubated with fluorescence-labelled anti-mouse IgG (LI-COR IRDye 680) and anti-human IgM (LI-COR IRDye 800) secondary antibodies. The membranes were scanned using a LI-COR Odyssey FC scanner, which reports results as arbitrary fluorescence units, providing CW700 and CW800 readings corresponding to recombinant protein abundance (anti-His6) and human serum IgM reactivity, respectively. A standard curve of His6-tagged human IgM, along with solvent and Ni-NTA-purified lysates from mock-transfected HEK293T cells, was used for standardization and background correction.

Generation and transfer of in vitro-transformed LCLs

$CD19^+$ B cells were either isolated from PBMCs of healthy donors or from splenocytes of humanized mice using magnetic beads for CD19 (Miltenyi) according to the manufacturer's instruction. A total of 5×10^5 $CD19^+$ cells per well were plated in a 96-well U-bottom plate in a total volume of 200 μl and cultured with luciferase-encoding EBV B95-8 supernatants with a multiplicity of infection of 0.5 in RPMI-1640 medium (Gibco) with 10% fetal bovine serum (Sigma), 1% L-glutamine (Thermo Fisher) and 1% penicillin–streptomycin (Thermo Fisher). Cells were maintained incubated at 37 °C under a 5% CO_2 humidified atmosphere. Half of the medium was removed and replaced with fresh medium if supernatant turned yellow. Once LCL clusters emerged, they were transferred into increasingly larger tissue culture plates. LCLs were regularly monitored for T-bet and CXCR3 expression by flow cytometry. All cell lines used in the experiments were tested monthly for mycoplasma contamination. $T\text{-}bet^+$ LCLs were FACS sorted (BD FACSAria III) into $CXCR3^+$ and $CXCR3^-$ populations to obtain a $T\text{-}bet^-$ and T-bet-expressing populations. Sorting was repeated if necessary. For the engraftment LCL transfer studies, 5×10^5 LCLs were engrafted into non-reconstituted BRGS-A2DR2 mice by intravenous tail-vein injection according to Soldan et al.[48]. The CXCR3 and CCR5 antagonist TAK-799 (MCE HY-13406) was i.p. injected daily starting 1 day post-LCL transfer until the end of the experiment at a concentration of 150 μg per mouse. TAK-799 was dissolved in 10% DMSO, 40% PEG-300, 5% Tween-80 and 45% saline. Natalizumab was injected once weekly i.p. at 10 mg kg^{-1}. Mice were imaged weekly by the IVIS Spectrum Imaging System (PerkinElmer). ROI quantifications were performed using the Living image software (v4.7).

Migration assay

For the transwell migration assay, LCLs were cultured for 2 days at a density of 2.5×10^5 cells per millilitre. T-bet-sorted LCLs were cultivated for 48 h at a density of 1×10^6 cells per millilitre. EBNA3B wild-type and knockout LCLs were cultivated for 24 h at a density of 1×10^6 cells per millilitre. Supernatant was collected and centrifuged for 5 min at 500*g* at 4 °C. T cells were isolated from whole-blood buffy coats using

CD3 microbeads according to the manufacturer's recommendations (Miltenyi). The transwell migration assay was adapted from Oner and Kobold[49]. In brief, 1×10^6 T cells were placed into the upper chamber in 70 µl R10, whereas the lower chamber was filled 225 µl of either LCL supernatant or R10 supplemented with human recombinant CCL3 (300-08-20UG, Thermo Fisher), human recombinant CCL4 (300-09-10UG, Thermo Fisher) and human recombinant CCL5 (300-06-20UG, Thermo Fisher) at a concentration of 1 µg ml^{-1}. As a positive control, R10 supplemented with 1 µg ml^{-1} human recombinant CXCL9 (300-26, Peprotech) was used, whereas R10 alone was used as the negative control. Neutralizing antibodies were used for CCL3 (AF-270-SP), CCL4 (AF-271-SP) and CCL5 (AF-278-SP; all RnD Systems), each at a concentration of 8 µg ml^{-1}. Supernatant was incubated with neutralizing antibodies for 1 h at 37 °C before co-culture with the isolated human T cells. For CXCR3 or CCR5 blocking, the CXCR3 antagonist TAK-779 (MCE HY-13406) was used at a concentration of 3 µM. TAK-799 was incubated with LCL supernatants and T cells for 1 h at 37 °C before co-culture with the isolated human T cells. Cells were given 4 h for migration before the remaining liquid in the upper chamber was removed and migrated cells in the lower chamber were analysed by flow cytometry. The gating strategy for the analysis of migrated T cells can be found in Extended Data Fig. 10c.

ELISA

Excess LCL supernatant, originating from the flask of LCLs seeded for the migration assay, was collected on the day of the transwell migration assay and stored at −20 °C. Production of human CCL3 was assessed by the human CCL3/MIP-1α DuoSet ELISA kit (DY270, RnD Systems). Production of human CCL4 was assessed using the human CCL4/MIP-1β DuoSet ELISA kit (DY271, RnD Systems). Production of human CCL5 was assessed using the Human CCL5/RANTES DuoSet ELISA kit (DY278, RnD Systems). Production of CXCL9 was assessed by the Human CXCL9 (MIG) ELISA kit (EHCXCL9, Invitrogen). Production of CXCL10 was assessed by the deluxe set human CXCL10 (IP-10) ELISA kit (439904, BioLegend). Production of TNF was assessed by the ELISA Flex: Human TNF (HRP) kit (3512-1H-6, Mabtech). ELISAs were performed according to the manufacturer's instructions, and cytokine production was calculated accordingly. The optical density was measured at 450 nm using the Tecan Infinite M200 Pro plate reader. The wavelength correction was set to 540 nm. For the NfL chain, plasma was collected via tail-vein bleeding before EBV infection and 6 weeks post-infection. Serum was collected at time point of euthanasia through the vena cava before perfusion. NF-Light Serum ELISA assay kit (20-8002 RUO) was used from Uman Diagnostics according to the manufacturer's instruction.

Histological staining

Tissue sections were formalin fixed and FFPE embedded. Staining of EBNA2 (clone PE2, Abcam) was carried out on a Leica BOND-III automated immunohistochemistry system with diaminobenzidine as substrate (Zytomed Systems). Areas for quantification were manually chosen based on location of EBNA expression. Three regions were selected from the meningeal area and parenchyma for quantification. Staining was measured on a Vectra3 automated quantitative pathology imaging system and analysed using Phenochart (v2.2.0) and InForm (v3.0.0) software (all from PerkinElmer).

Graphical illustrations

The graphical illustrations in Figs. 1a, 3a and 5a and Extended Data Fig. 7f were generated with Adobe Illustrator (v29.3.1).

Statistical analysis

The MWU test was used to analyse unpaired data with non-Gaussian distribution. Correlative analyses were assessed by non-parametric Spearman correlation. Non-parametric data with more than two groups were compared by Dunn's multiple comparison test following Kruskall–Wallis test. A $P < 0.05$ was considered statistically significant. All statistics were computed with GraphPad Prism (v10.2.3; GraphPad Software) unless noted otherwise and details can be found in the figures or in corresponding legends.

Reporting summary

Further information on research design is available in the Nature Portfolio Reporting Summary linked to this article.

Data availability

The scRNA-seq datasets analysed in this study are available from the Gene Expression Omnibus (Fig. 3; GSE299939) and Zenodo[50] (Extended Data Fig. 5; https://doi.org/10.5281/zenodo.15602185). The multiplex immunofluorescence images are also available to download from Zenodo[51] (https://doi.org/10.5281/zenodo.15599580).

Code availability

The code used to analyse scRNA-seq data and multiplex immunofluorescence images can be found via GitHub (https://github.com/EannaFennell/EBV-induces-CNS-homing-of-B-cells-attracting-inflammatory-T-cells). The package used for multiplex immunofluorescence analysis is also available from GitHub (https://github.com/EannaFennell/MISSILe).

44. Sahir, F., Mateo, J. M., Steinhoff, M. & Siveen, K. S. Development of a 43 color panel for the characterization of conventional and unconventional T-cell subsets, B cells, NK cells, monocytes, dendritic cells, and innate lymphoid cells using spectral flow cytometry. *Cytometry A* https://doi.org/10.1002/cyto.a.24288 (2020).
45. Puccio, S. et al. CRUSTY: a versatile web platform for the rapid analysis and visualization of high-dimensional flow cytometry data. *Nat. Commun.* **14**, 5102 (2023).
46. Adhikary, D. et al. Immunodominance of lytic cycle antigens in Epstein–Barr virus-specific CD4$^+$ T cell preparations for therapy. *PLoS ONE* **2**, e583 (2007).
47. Nuckel, J. et al. Association between IgG responses against the nucleocapsid proteins of alphacoronaviruses and COVID-19 severity. *Front. Immunol.* **13**, 889836 (2022).
48. Soldan, S. S. et al. Epigenetic plasticity enables CNS-trafficking of EBV-infected B lymphocytes. *PLoS Pathog.* **17**, e1009618 (2021).
49. Oner, A. & Kobold, S. Transwell migration assay to interrogate human CAR-T cell chemotaxis. *STAR Protoc.* **3**, 101708 (2022).
50. Fennell, E. Single-cell RNA and B cell receptor sequencing processed data from EBV-infected and PBS humanised BRGS-A2DR2 mice. *Zenodo* https://doi.org/10.5281/zenodo.15602185 (2025).
51. Fennell, E. Multiplex immunofluorescence images of spleens from EBV-infected BRGS-A2DR2 mice. *Zenodo* https://doi.org/10.5281/zenodo.15599580 (2025).

Acknowledgements We thank the Functional Genomics Center Zürich of the University of Zürich and ETH Zurich, and in particular Q. Zhang, for support on the genomics analyses; K. Gehrmann for technical support with the humanized mice; J. Fullin for creating the graphical illustrations featured in the figures; and F.L. thanks L. Yuka for ongoing support. This research was in part financially supported by the Swiss National Science Foundation (310030_204470/1, 310030L_197952/1 and CRSII_222718_10000065), Cancer Research Switzerland (KFS-5896-08-2023-R), the Swiss MS Society (2023-17), the Swiss State Secretariat for Education, Research and Innovation for EU Horizon BEHIND-MS, CRPP-ImmunoCure of the University of Zürich, the Sobek Foundation, the Swiss Vaccine Research Institute, the Vontobel Foundation, Roche, Novartis and Viracta. L.R. was supported by career advancement grants from the University of Zurich (Forschungskredit, FK-21-034). É.F. is funded by HORIZON-TMA-MSCA-PF-GF (no. 101110227). G.F. is funded by Next Generation EU — NRRP M6C2 — Investment 2.1 Enhancement and strengthening of biomedical research in the NHS — PNRR-MCNT2-2023-12378122; CUP: C43C23000880006.

Author contributions F.L., I.P., É.F., S.S., L.R. and J. Mietz performed the in vivo experiments. F.L., I.P., E.B. and C.C. performed the in vitro EBV infection and transwell migration experiments. E.B. and A.M. performed the ChipCytometry experiments. É.F. and P.G. performed the bioinformatics analysis. I.L.-P., L.B., A.G., K.E. and J.S. performed light-sheet microscopy. M.L. and J. Mautner performed serological assays for viral and autoantigen recognition by IgM. G.P. and G.F. performed HLA typing. C.M. supervised the study. F.L., E.B. and C.M. wrote the first draft of the manuscript. All authors edited the manuscript.

Competing interests The authors declare no competing interests.

Additional information

Supplementary information The online version contains supplementary material available at https://doi.org/10.1038/s41586-025-09378-0.

Correspondence and requests for materials should be addressed to Christian Münz.

Peer review information *Nature* thanks Deepak Rao and the other, anonymous, reviewer(s) for their contribution to the peer review of this work. Peer reviewer reports are available.

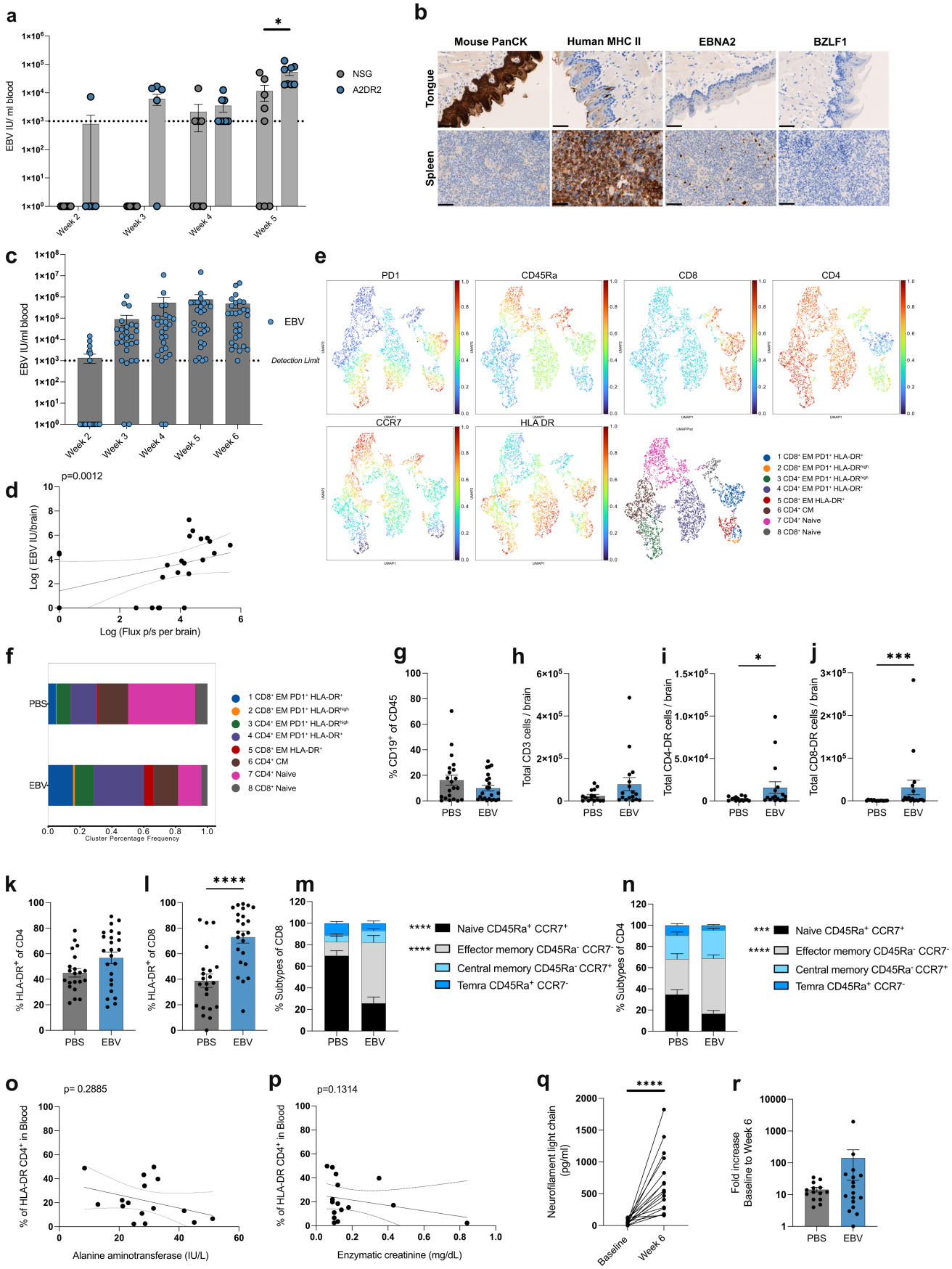

Extended Data Fig. 1 | See next page for caption.

Extended Data Fig. 1 | T cell infiltration into the CNS and associated NfL release. a, Weekly blood viral loads (IU/ml blood) of EBV-infected humanized NSG and BRGS-A2DR2 mice (p-value = 0.010256; NSG = 8, BRGS-A2DR2 = 8). **b**, IHC staining of EBV-infected BRGS-A2DR2 tongue and spleen sections, scale bar=100µm. **c**, Weekly blood viral loads (IU/ml) of EBV-infected humanized BRGS-A2DR2 mice (n = 28). **d**, Correlation between brain EBV viral load and bioluminescent signal (n = 23). **e**, UMAP of marker expression by T cell populations. **f**, Percentage of the indicated T cell differentiation subpopulations. **g**, Frequency of $CD19^+$ B cells in brains of PBS or EBV-infected mice (PBS n = 20, EBV n = 23). **h-j**, Total numbers of $CD3^+$, activated $HLA\text{-}DR^+CD4^+$ (p-value = 0.0435), and activated $HLA\text{-}DR^+CD8^+$ T cells (p-value = 0.0002) in brains of PBS or EBV-infected mice (PBS n = 15, EBV n = 15). **k-l**, Frequencies of $HLA\text{-}DR^+CD8^+$ (p-value < 0.0001) and $HLA\text{-}DR^+CD4^+$ T cells of PBS or EBV-infected mouse spleens (PBS n = 20, EBV n = 23). **m-n**, Frequency of $CD4^+$ (naïve p-value = 0.0001, effector memory p-value < 0.0001) and $CD8^+$ (naïve p-value < 0.0001, effector memory p-value < 0.0001) T cell differentiation subtypes of PBS or EBV-infected mouse spleens. **o-p**, Correlation between $HLA\text{-}DR^+CD4^+$ T cells and alanine aminotransferase activity or enzymatic creatinine concentrations in blood (n = 18). **q**, ELISA of neurofilament light chain (NfL) in plasma before (Baseline) and 6 weeks post-EBV infection (Week 6; p-value < 0.0001). **r**, Fold increase of plasma NfL levels before and 6 weeks post-EBV infection or PBS injection. For all correlations, solid line represents trend line obtained by linear regression, the dotted lines indicate 95% confidence bands, two-tailed p-value by Spearman correlation. Unless otherwise indicated, p-values by two-tailed MWU test. a, was generated from one experiment using mice reconstituted from one human $CD34^+$ hematopoietic progenitor cells donor. b-m, were generated from 3 independent experiments with 4 donors. d, was created with crusty.humanitas.it. Error bar indicates SEM; each dot represents one single animal. *p < 0.05, **p < 0.01, ***p < 0.001, ****p < 0.0001.

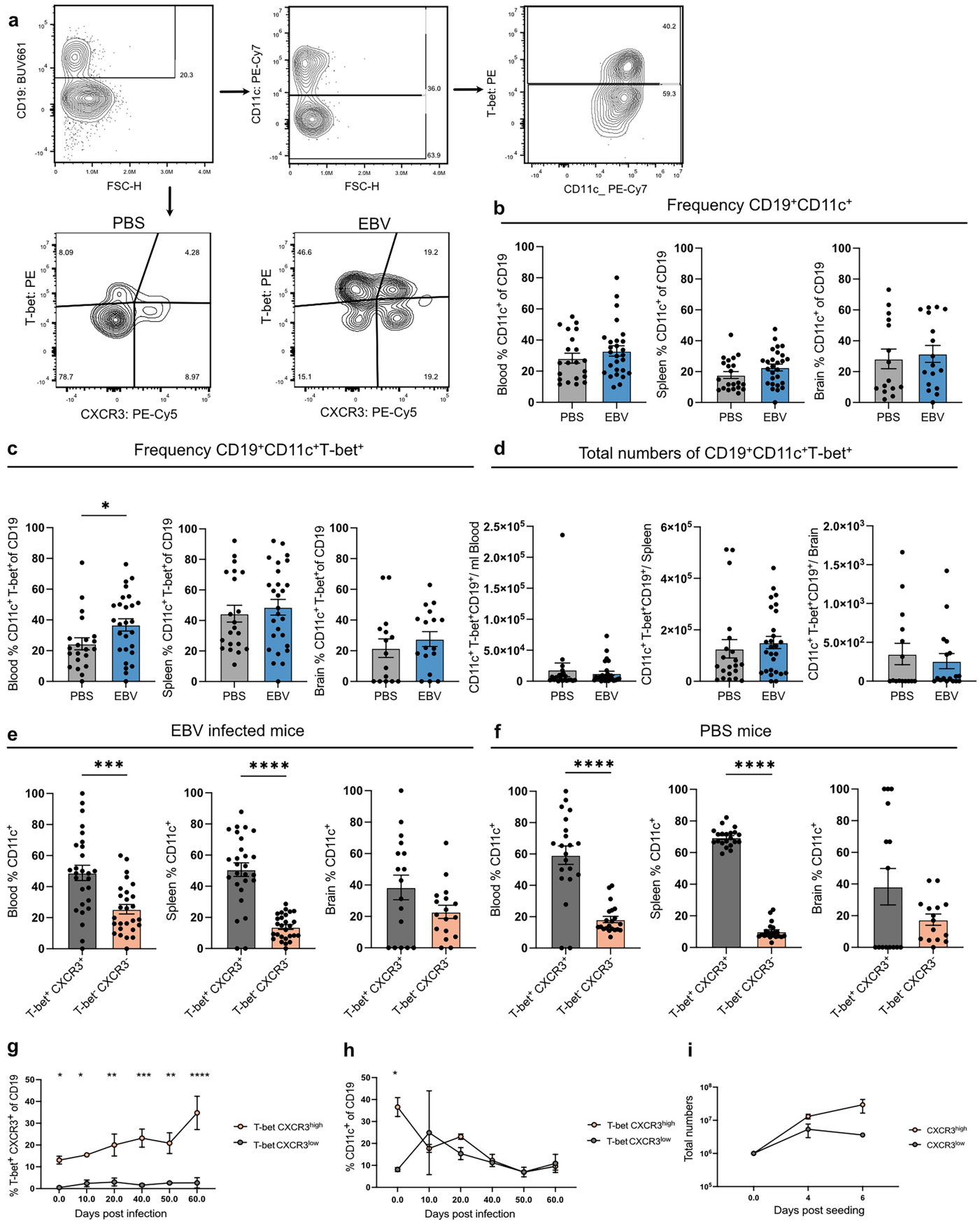

Extended Data Fig. 2 | See next page for caption.

Extended Data Fig. 2 | Characteristics and origin of EBV expanded T-bet$^+$CXCR3$^+$ B cells. a, Representative flow cytometric contour plots of T-bet$^+$CXCR3$^+$ and T-bet$^+$CD11c$^+$ B cell gating of splenocytes from PBS or EBV-infected humanized mice. **b**, Frequencies of CD19$^+$CD11c$^+$ B cells in blood, spleen and brains of PBS or EBV-infected humanized mice (PBS n = 21, EBV n = 28). **c**, Frequencies of CD19$^+$CD11c$^+$T-bet$^+$ B cells in blood (p-value = 0.0277), spleen and brains of PBS or EBV-infected humanized mice (PBS n = 21, EBV n = 28). **d**, Total numbers of CD19$^+$T-bet$^+$CD11c$^+$ B cells in blood, spleen and brains of PBS or EBV-infected humanized mice (PBS n = 21, EBV n = 28). **e**, Frequency of T-bet$^+$CXCR3$^+$ and T-bet$^-$CXCR3$^-$ cells among CD11c$^+$ B cells in blood (p-value = 0.0004), spleen (p-value < 0.0001) and brains of EBV infected mice. **f**, Frequency of T-bet$^+$CXCR3$^+$ and T-bet$^-$CXCR3$^-$ cells among CD11c$^+$ B cells in blood (p-value < 0.0001), spleen (p-value < 0.0001) and brains of PBS mice. **g**, In vitro EBV infection of CXCR3$^+$ and CXCR3$^-$ B cells monitoring T-bet/CXCR3 co-expression frequency over time (p-values from left to right: 0.0211, 0.0160, 0.0016, 0.0007, 0.0039, <0.0001). **h**, In vitro EBV infection of CXCR3$^+$ and CXCR3$^-$ B cells monitoring CD11c frequency over time (p-value = 0.0461). **i**, Growth assay of established LCLs derived from CXCR3$^+$ or CXCR3$^-$ B cells over time depicted as total numbers. g-i, p-values were calculated using mixed-effects model with Geisser-Greenhouse correction followed by Sidak's multiple comparisons test. Unless otherwise indicated, p-values were calculated using the two-tailed MWU test. Data from figures b-f, was generated from 5 independent experiments with mice reconstituted from 6 different human CD34$^+$ hematopoietic progenitor cells donors. Error bar indicates SEM; each dot represents one single animal. Data from Figure g-i was generated from 3 independent experiment using 3 B cells donors. Error bar indicates SEM; dots represent mean of all 3 donors. *p < 0.05, **p < 0.01, ***p < 0.001, ****p < 0.0001.

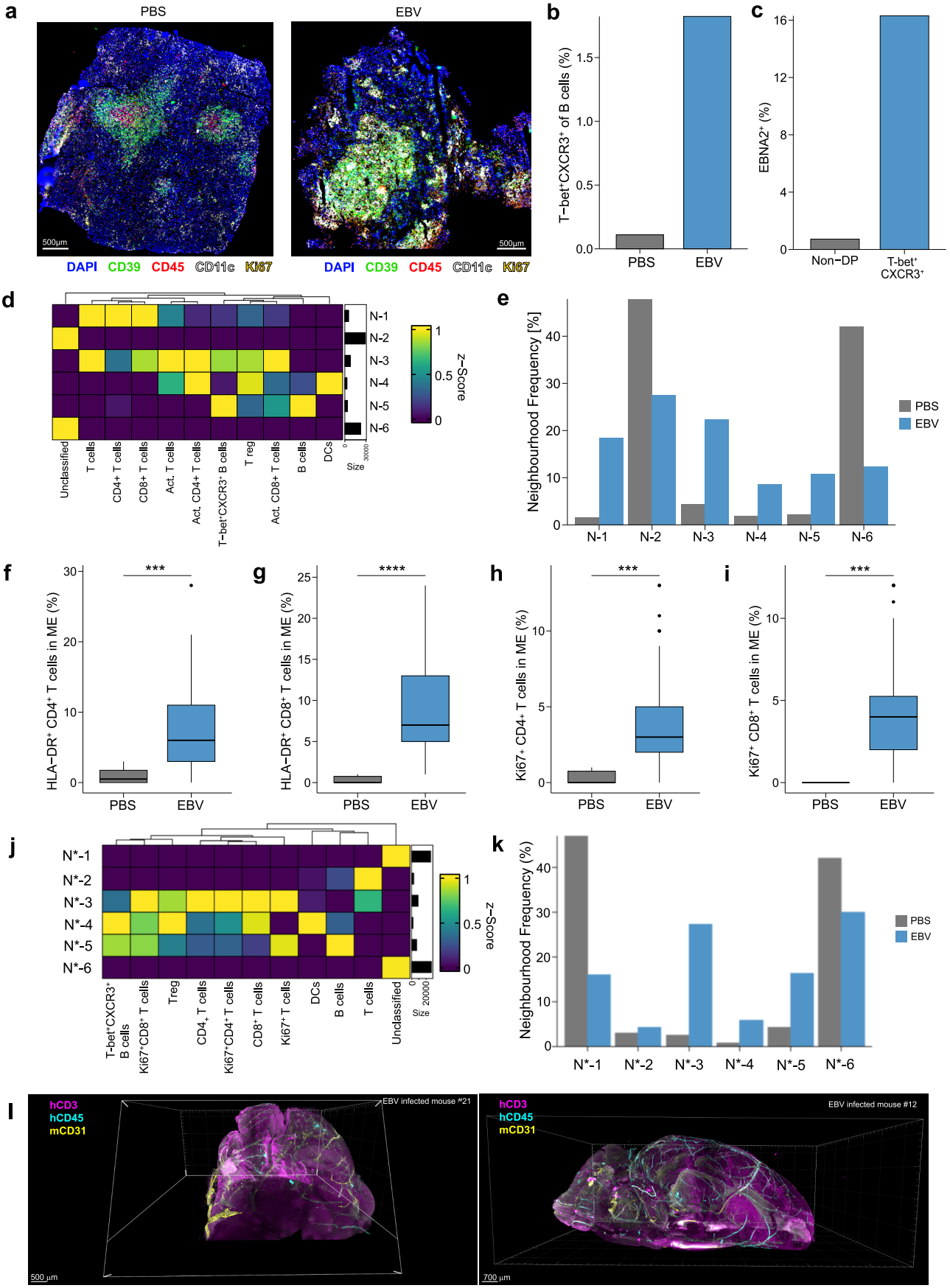

Extended Data Fig. 3 | See next page for caption.

Extended Data Fig. 3 | Spatial analysis of T-bet$^+$CXCR3$^+$ B cells and activated T cells. a, ChipCytometry of DNA (Helix-NP), CD39, CD45, CD11c and Ki67 on splenic section of PBS and EBV-infected mice. Scale bar=500µm. **b**, Frequency of T-bet$^+$CXCR3$^+$ of total B cells in spleen of PBS and EBV-infected mice (PBS n = 1, EBV n = 1). **c**, Frequency of EBNA2$^+$ among T-bet$^+$CXCR3$^+$ and non-T-bet$^+$CXCR3$^+$ (other) B cells in spleen of EBV infected mice (PBS n = 1, EBV n = 1). **d**, Cell type enrichment per calculated tissue neighbourhood using HLA-DR as activation marker and **e**, frequency of respective tissue neighbourhoods (N-1 to N-5) in PBS and EBV-infected spleens (PBS n = 1, EBV n = 1). **f-g**, Frequency of activated CD4$^+$ and CD8$^+$ T cells (HLA-DR$^+$) in the immediate microenvironment (ME; 100µm) of T-bet$^+$CXCR3$^+$ B cells in PBS and EBV-infected spleens (PBS n = 6, EBV n = 92 microenvironments of 1 experiment). P-values were calculated using two-sided MWU test (p-values = 0.00062 & 0.000045 respectively). **h-i**, Frequency of proliferative CD4$^+$ and CD8$^+$ T cells (Ki67$^+$) in the immediate microenvironment (100µm) of T-bet$^+$CXCR3$^+$ B cells in PBS and EBV-infected (PBS n = 6, EBV n = 92 microenvironments of 1 experiment). P-values were calculated using two-sided MWU test (p-values = 0.0001 & 0.00014 respectively). Box plots define the medium value (centre), the interquartile range (25th and 75th percentiles) as the boundaries of the box and whiskers which extend to 1.5 times the 25th and 75th percentiles. Outliers outside the boundaries of the whiskers are displayed as individual points. *$p < 0.05$, **$p < 0.01$, ***$p < 0.001$, ****$p < 0.0001$. **j**, Cell type enrichment per calculated tissue neighbourhood using Ki67 as a T cell proliferation marker and **k**, frequency of respective tissue neighbourhoods (N*-1 to N*-6) in PBS and EBV-infected spleens. **l**, 3D multiplex imaging by light sheet microscopy of cleared brains of two EBV-infected mice (EBV n = 3, PBS n = 1) stained for human CD3 (magenta), human CD45 (cyan) and mouse CD31 (yellow).

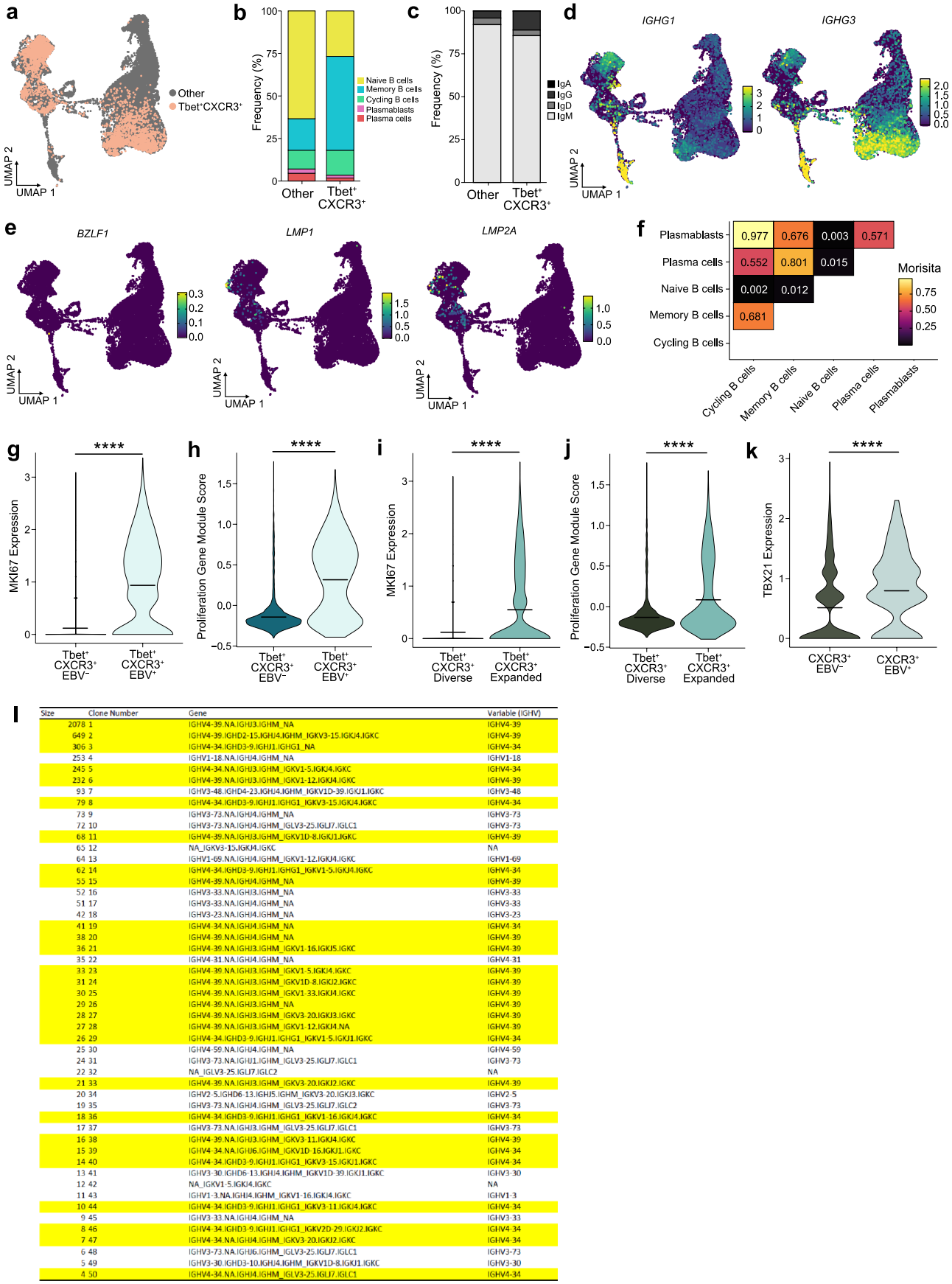

l

Size	Clone Number	Gene	Variable (IGHV)
2078	1	IGHV4-39.NA.IGHJ3.IGHM_NA	IGHV4-39
649	2	IGHV4-39.IGHD2-15.IGHJ4.IGHM_IGKV3-15.IGKJ4.IGKC	IGHV4-39
306	3	IGHV4-34.IGHD3-9.IGHJ1.IGHG1_NA	IGHV4-34
253	4	IGHV1-18.NA.IGHJ4.IGHM_NA	IGHV1-18
245	5	IGHV4-34.NA.IGHJ3.IGHM_IGKV1-5.IGKJ4.IGKC	IGHV4-34
232	6	IGHV4-39.NA.IGHJ3.IGHM_IGKV1-12.IGKJ4.IGKC	IGHV4-39
93	7	IGHV3-48.IGHD4-23.IGHJ4.IGHM_IGKV1D-39.IGKJ1.IGKC	IGHV3-48
79	8	IGHV4-34.IGHD3-9.IGHJ1.IGHG1_IGKV3-15.IGKJ4.IGKC	IGHV4-34
73	9	IGHV3-73.NA.IGHJ4.IGHM_NA	IGHV3-73
72	10	IGHV3-73.NA.IGHJ4.IGHM_IGLV3-25.IGLJ7.IGLC1	IGHV3-73
68	11	IGHV4-39.NA.IGHJ3.IGHM_IGKV1D-8.IGKJ1.IGKC	IGHV4-39
65	12	NA_IGKV3-15.IGKJ4.IGKC	NA
64	13	IGHV1-69.NA.IGHJ4.IGHM_IGKV1-12.IGKJ4.IGKC	IGHV1-69
62	14	IGHV4-34.IGHD3-9.IGHJ1.IGHG1_IGKV1-5.IGKJ4.IGKC	IGHV4-34
55	15	IGHV4-39.NA.IGHJ4.IGHM_NA	IGHV4-39
52	16	IGHV3-33.NA.IGHJ3.IGHM_NA	IGHV3-33
51	17	IGHV3-33.NA.IGHJ4.IGHM_NA	IGHV3-33
42	18	IGHV3-23.NA.IGHJ4.IGHM_NA	IGHV3-23
41	19	IGHV4-34.NA.IGHJ4.IGHM_NA	IGHV4-34
38	20	IGHV4-39.NA.IGHJ4.IGHM_NA	IGHV4-39
36	21	IGHV4-39.NA.IGHJ3.IGHM_IGKV1-16.IGKJ5.IGKC	IGHV4-39
35	22	IGHV4-31.NA.IGHJ4.IGHM_NA	IGHV4-31
33	23	IGHV4-39.NA.IGHJ3.IGHM_IGKV1-5.IGKJ4.IGKC	IGHV4-39
31	24	IGHV4-39.NA.IGHJ3.IGHM_IGKV1D-8.IGKJ2.IGKC	IGHV4-39
30	25	IGHV4-39.NA.IGHJ3.IGHM_IGKV1-33.IGKJ4.IGKC	IGHV4-39
29	26	IGHV4-39.NA.IGHJ3.IGHM_NA	IGHV4-39
28	27	IGHV4-39.NA.IGHJ3.IGHM_IGKV3-20.IGKJ3.IGKC	IGHV4-39
27	28	IGHV4-39.NA.IGHJ3.IGHM_IGKV1-12.IGKJ4.NA	IGHV4-39
26	29	IGHV4-34.IGHD3-9.IGHJ1.IGHG1_IGKV1-5.IGKJ1.IGKC	IGHV4-34
25	30	IGHV4-59.NA.IGHJ4.IGHM_NA	IGHV4-59
24	31	IGHV3-73.NA.IGHJ1.IGHM_IGLV3-25.IGLJ7.IGLC1	IGHV3-73
22	32	NA_IGLV3-25.IGLJ7.IGLC2	NA
21	33	IGHV4-39.NA.IGHJ3.IGHM_IGKV3-20.IGKJ2.IGKC	IGHV4-39
20	34	IGHV2-5.IGHD6-13.IGHJ5.IGHM_IGKV3-20.IGKJ3.IGKC	IGHV2-5
19	35	IGHV3-73.NA.IGHJ4.IGHM_IGLV3-25.IGLJ7.IGLC2	IGHV3-73
18	36	IGHV4-34.IGHD3-9.IGHJ1.IGHG1_IGKV1-16.IGKJ4.IGKC	IGHV4-34
17	37	IGHV3-73.NA.IGHJ3.IGHM_IGLV3-25.IGLJ7.IGLC1	IGHV3-73
16	38	IGHV4-39.NA.IGHJ3.IGHM_IGKV3-11.IGKJ4.IGKC	IGHV4-39
15	39	IGHV4-34.NA.IGHJ6.IGHM_IGKV1D-16.IGKJ1.IGKC	IGHV4-34
14	40	IGHV4-34.IGHD3-9.IGHJ1.IGHG1_IGKV3-15.IGKJ1.IGKC	IGHV4-34
13	41	IGHV3-30.IGHD6-13.IGHJ4.IGHM_IGKV1D-39.IGKJ1.IGKC	IGHV3-30
12	42	NA_IGKV1-5.IGKJ4.IGKC	NA
11	43	IGHV1-3.NA.IGHJ4.IGHM_IGKV1-16.IGKJ4.IGKC	IGHV1-3
10	44	IGHV4-34.IGHD3-9.IGHJ1.IGHG1_IGKV3-11.IGKJ4.IGKC	IGHV4-34
9	45	IGHV3-33.NA.IGHJ4.IGHM_NA	IGHV3-33
8	46	IGHV4-34.IGHD3-9.IGHJ1.IGHG1_IGKV2D-29.IGKJ2.IGKC	IGHV4-34
7	47	IGHV4-34.NA.IGHJ4.IGHM_IGKV3-20.IGKJ2.IGKC	IGHV4-34
6	48	IGHV3-73.NA.IGHJ6.IGHM_IGLV3-25.IGLJ7.IGLC1	IGHV3-73
5	49	IGHV3-30.IGHD3-10.IGHJ4.IGHM_IGKV1D-8.IGKJ1.IGKC	IGHV3-30
4	50	IGHV4-34.NA.IGHJ4.IGHM_IGLV3-25.IGLJ7.IGLC1	IGHV4-34

Extended Data Fig. 4 | See next page for caption.

Extended Data Fig. 4 | Transcriptional characteristics of T-bet$^+$CXCR3$^+$ B cells. a, UMAP of T-bet$^+$CXCR3$^+$ among splenic B cells of EBV-infected humanized mice by scRNA-seq. **b-c**, Stacked bar plots showing (left) the CD19$^+$ B cell population frequency and (right) immunoglobulin isotype distribution within T-bet$^+$CXCR3$^+$ and non-T-bet$^+$CXCR3$^+$ (other) cells. **d**, Expression of indicated Ig isotypes and **e**, expression of indicated EBV transcripts. **f**, Heatmap of shared clones between B cell subtypes with Morisita overlap index. **g-h**, Violin plot of expression of MKI67 (adjusted p-value = 1.41e-260) and pro-proliferative gene module (MKI67, PCNA, TOP2A, CCNB1, CCNB2, CDK1; adjusted p-value = 2.64e-157) between infected (EBV$^+$) and un-infected (EBV$^-$) T-bet$^+$CXCR3$^+$ B cells. **i-j**, Violin plot of expression of MKI67 (adjusted p-value = 2.105e-86) and pro-proliferative gene module (MKI67, PCNA, TOP2A, CCNB1, CCNB2, CDK1; adjusted p-value = 2.86e-32) between clonally expanded and diverse BCR expressing T-bet$^+$CXCR3$^+$ B cells. **k**, Violin plot of expression of TBX21 between infected (EBV$^+$) and un-infected (EBV$^-$) CXCR3$^+$ B cells (adjusted p value = 1.706e-29). **l**, IGHV gene expression among the top 50 expanded B cell clones. IGHV4-34 and IGHV4-39 expressing clones are highlighted. The black line defines the mean expression of each group from g-j. P-values for differential gene expression analysis between groups were calculated using the two-sided MWU test. *$p < 0.05$, **$p < 0.01$, ***$p < 0.001$, ****$p < 0.0001$.

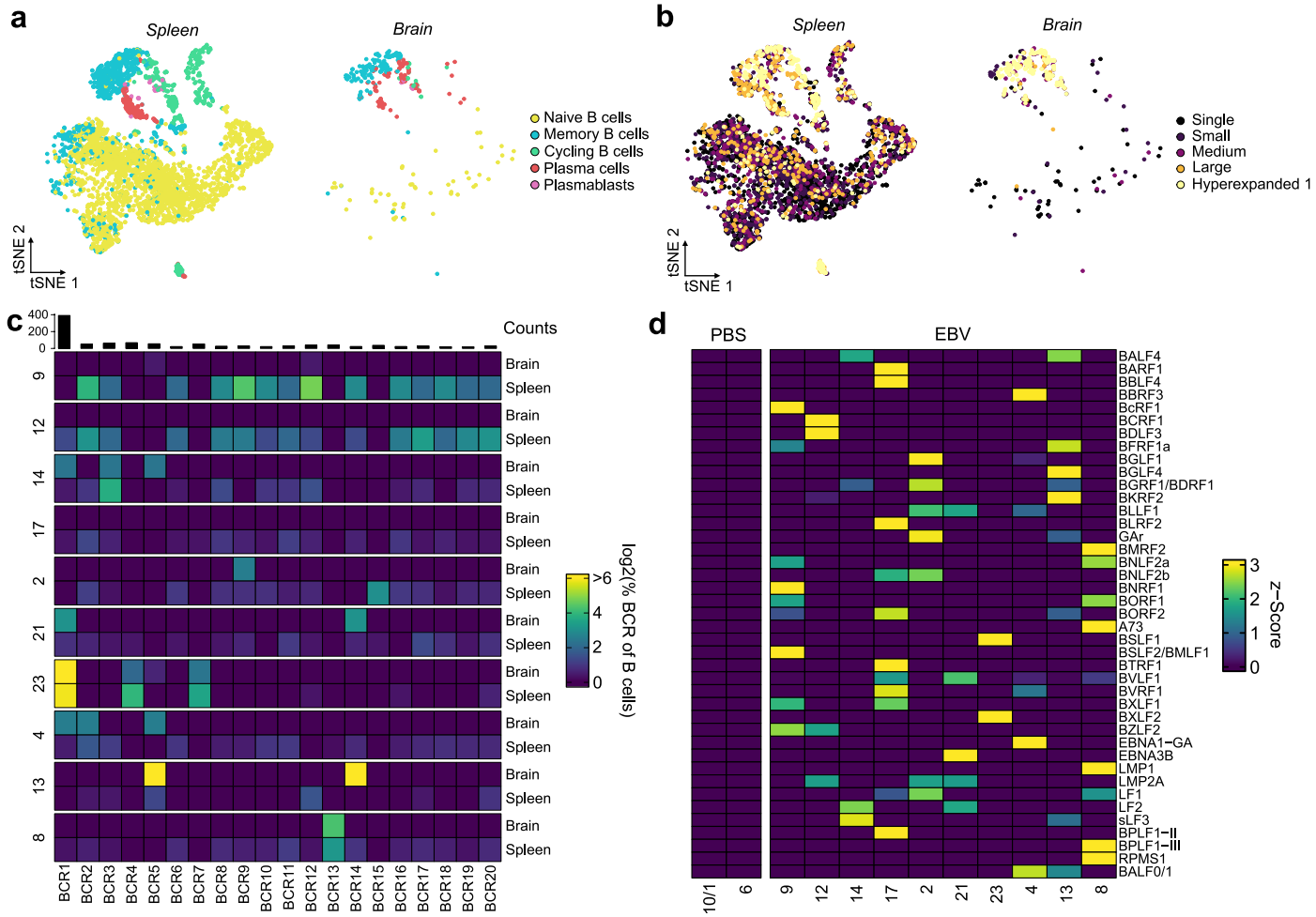

Extended Data Fig. 5 | CNS accumulation and EBV antigen recognition of oligoclonally EBV expanded B cells. a, tSNE of single cell RNA sequencing (scRNA-seq) of sorted CD19$^+$ B cells from spleen and perfused brains of EBV infected humanized BRGS-A2DR2 mice (n = 10) 6 weeks after EBV infection with manually annotated B cell differentiation clusters. **b**, BCR receptor clonality analysis. Clones were defined by Single (0 < X < = 1), Small (1 < X < = 5), Medium (5 < X < = 20), Large (20 < X < = 50), Hyperexpanded 1 (50 < X < = 200). **c**, Z-scored heatmap of 20 most expanded BCRs in matched perfused brain and spleen samples of the 10 analyzed mice (mouse #9, 12, 14, 17, 2, 21, 23, 4, 13, 8). **d**, Z-scored heatmap of IgM responses to the indicated EBV gene products in blood plasma of the same 10 by scRNA-seq analyzed EBV infected mice and three PBS controls (mouse #1, 6, 10). Plasma of mouse 1 and 10 was pooled due to low individual blood plasma volume.

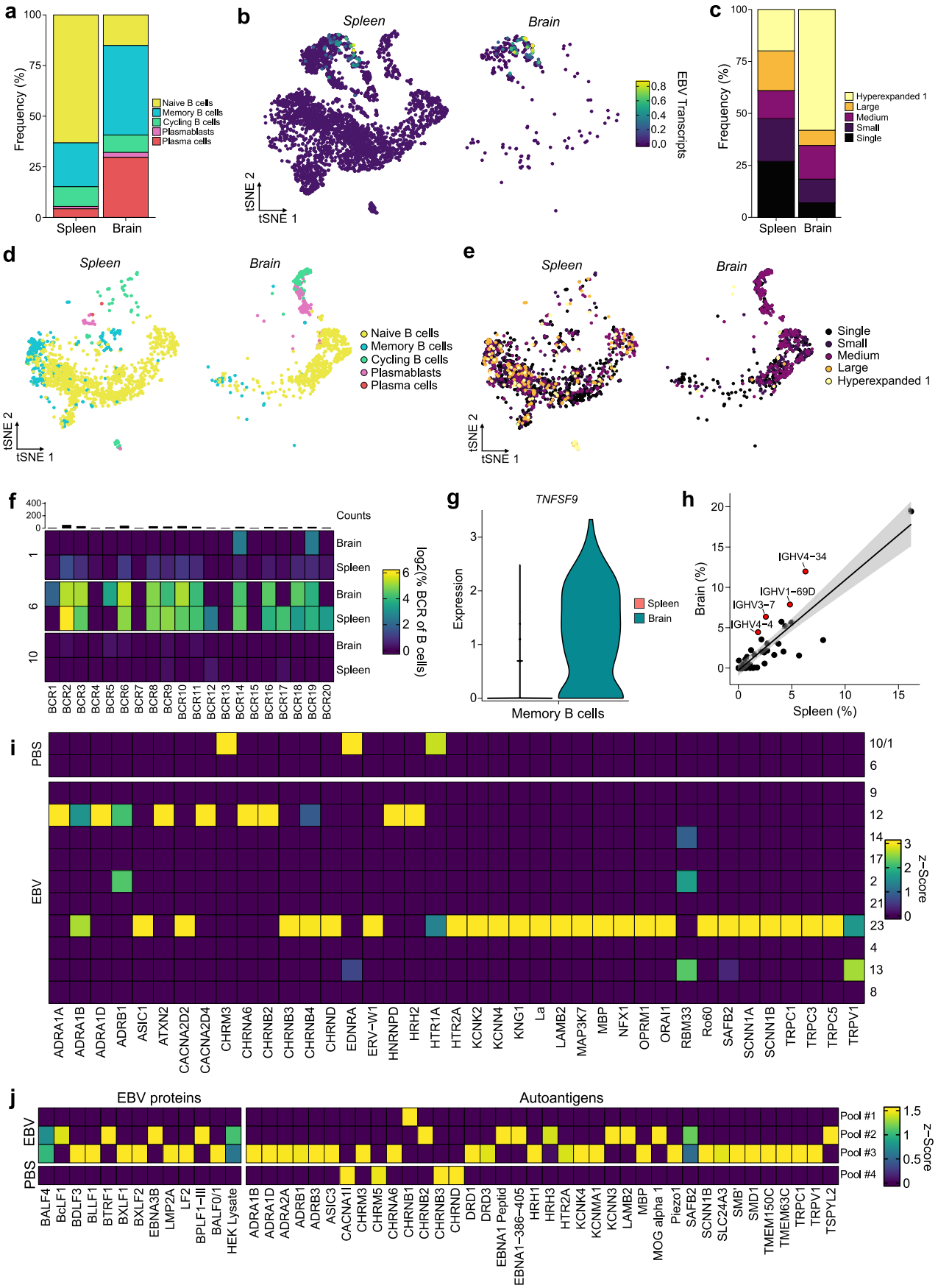

Extended Data Fig. 6 | See next page for caption.

Extended Data Fig. 6 | Oligoclonal B cell expansion and autoantigen recognition after EBV infection. a, Stacked bar plot showing B cell population frequency in spleen and brain of EBV-infected mice. **b**, tSNE of combined expression of all EBV transcripts split by organ of origin (spleen and brain). **c**, Stacked bar plot showing clonality distribution of non-naïve clusters (i.e. memory B cells, cycling B cells, plasmablasts & plasma cells) in spleen and brain of EBV-infected mice only. **d-e**, tSNE of sorted $CD19^+$ B cell population colored by B cell populations (d) and BCR clonality (e), split by organ of origin (spleen and brain) of PBS mice only. Clones were defined by Single ($0 < X <= 1$), Small ($1 < X <= 5$), Medium ($5 < X <= 20$), Large ($20 < X <= 50$), Hyperexpanded 1 ($50 < X <= 200$). **f**, Shared spleen and brain BCR clones heatmap of individual PBS mice (most abundant 20 BCRs are plotted). BCR frequencies were calculated from total B cells per organ per mouse and were log2 normalised. **g**, TNFSF9 (encodes 4-1BBL/CD137L) expression in spleen and brain memory B cells. **h**, Distribution of IGHV gene in spleen versus brain B cells. The linear regression line (which represents the fitted values/mean predicted response from the linear model) and 95% confidence interval (in grey) are plotted. **i**, Blood plasma IgM antibody specificities against known autoantigens of all mice used for the scRNA-seq analysis. **j**, Replicate serum antibody specificities against EBV proteins and known autoantigens from pooled mice of previous EBV infection experiments. Pool #1 consisted of 2 mice (EBV infected), pool #2 and #3 consisted of 3 mice each (EBV infected), pool #4 from 3 mice (PBS controls). Pooled mice originated from individual $CD34^+$ hematopoietic progenitor cell donors.

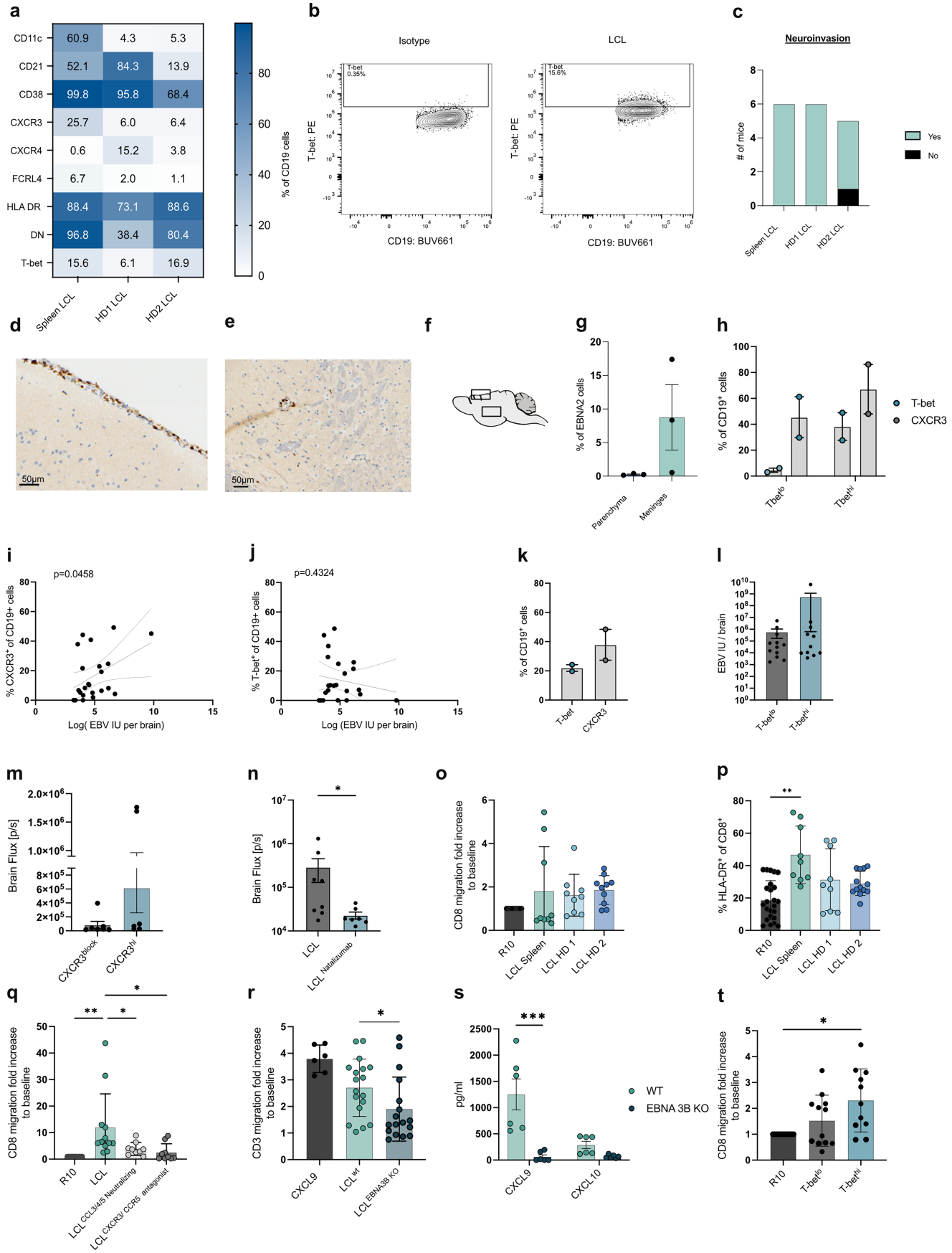

Extended Data Fig. 7 | See next page for caption.

Extended Data Fig. 7 | CNS homing and T cell attraction by EBV infected T-bet$^+$CXCR3$^+$ B cells. a, Heatmap of indicated LCL marker frequency. **b**, Representative T-bet staining on LCL. **c**, Total mouse numbers with neuroinvasion. **d-e**, IHC staining of EBNA2 in indicated (**f**) meningeal and parenchymal brain areas. Scale bar=50µm. **g**, EBNA2$^+$ cell frequency (n = 3 per region). **h**, T-bet and CXCR3 frequency of T-bet^{lo} and T-bet^{hi}. **i**, Correlation between blood CXCR3 frequency and neuroinvasion (n = 23). **j**, Correlation between blood T-bet frequency and neuroinvasion (n = 23). **k**, T-bet and CXCR3 frequency of LCL used for CXCR3 inhibition (TAK-779). **l**, EBV viral loads (IU/brain; T-bet^{lo} n = 12, T-bet^{hi} n = 11). **m-n**, Brain viral loads by bioluminescence after CXCR3 inhibition (TAK-779; PBS n = 6, CXCR3 antagonist n = 7) or Natalizumab treatment (p-value = 0.0401; PBS n = 8, Natalizumab n = 7). **o**, Transwell migration assays with indicated LCL supernatants. **p**, Frequency of migrated HLA-DR$^+$CD8$^+$ T cells (LCL spleen p-value = 0.0015). **q**, Transwell migration assays with LCL supernatant (p-value = 0.0015) with CCL3/4/5 (p = 0.0366) or CXCR3/CCR5 inhibition (TAK-779; p-value = 0.0125). **r**, Transwell migration assays with CXCL9$^+$ medium or wild-type vs. EBNA3B deficient LCL supernatants (p-value = 0.0292). **s**, ELISA on wild-type and EBNA3B deficient LCL supernatants (p-value = 0.0004). **t**, Transwell migration assays with T-bet^{hi} (p-value = 0.0372) or T-bet^{lo} LCL supernatants. Each dot represents one well. For all correlations, solid line represents trend line obtained by linear regression, the dotted lines indicate 95% confidence bands two-tailed p-value was calculated using Spearman correlation. Data from figure a-c was generated from 3 independent experiments and h-n from 2 independent experiments with 2 LCL donors. o-r and t were tested with =>3 T cells donors. p-values were calculated using one-way ANOVA with Dunnett's multiple comparison test. s, was generated using supernatant of n = 3 wild-type (WT) and n = 3 EBNA3B deficient LCLs (EBNA3A KO) in 2 independent experiments, p-value was calculated with two-way ANOVA followed by Sidak's multiple comparisons test. Error bar indicates SEM. *p < 0.05, **p < 0.01, ***p < 0.001, ****p < 0.0001.

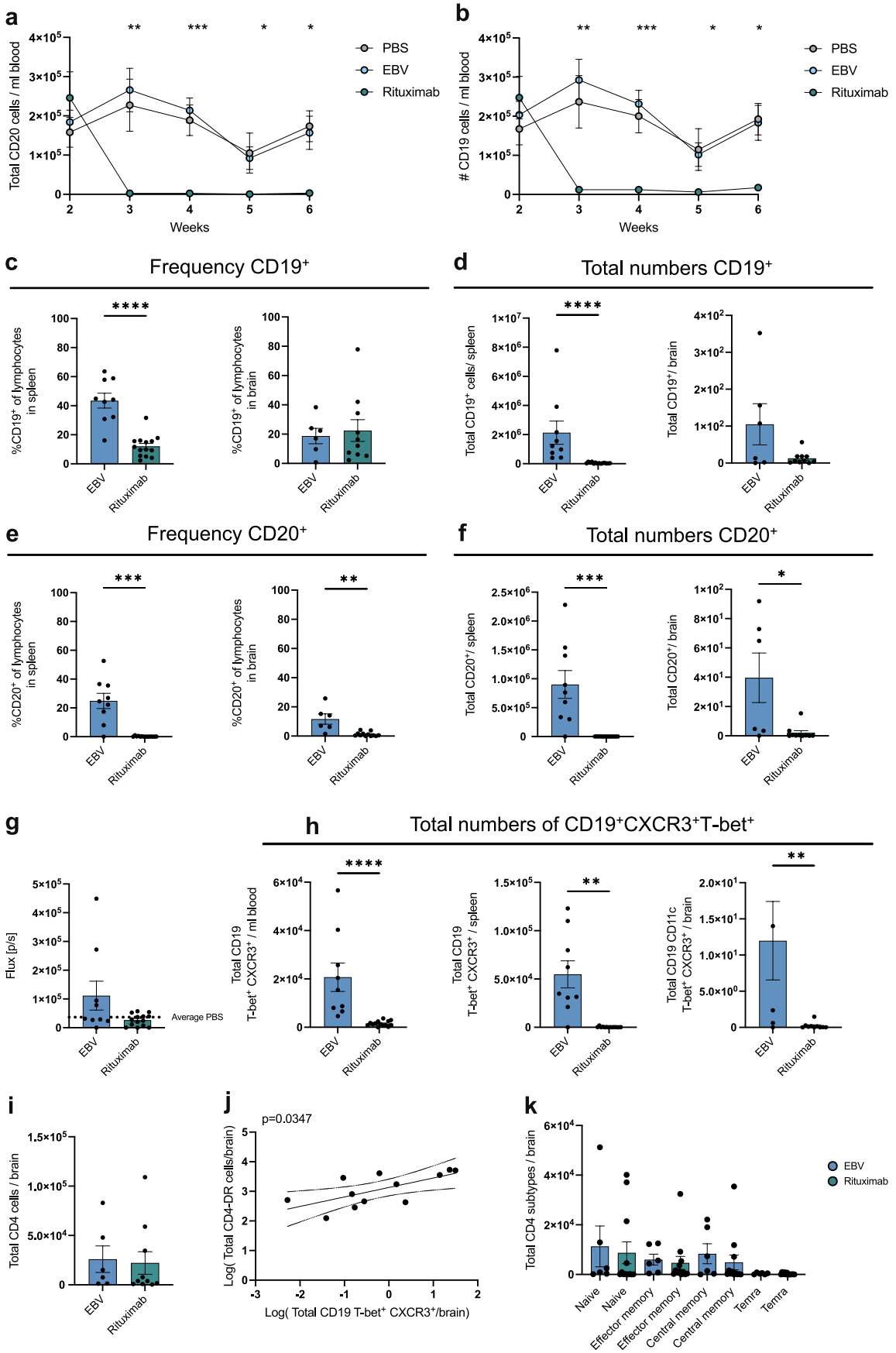

Extended Data Fig. 8 | See next page for caption.

Extended Data Fig. 8 | CD20 targeted B cell depletion. a-b, Weekly total numbers of $CD45^+CD19^+$ or $CD20^+$ B cells in blood of EBV-infected mice with and without Rituximab treatment (PBS n = 5, EBV n = 4, Rituximab n = 7). p-values from left to right: CD20:0.0026, 0.0003,0.029,0.0120CD19: 0.0014,0.0004.0.0235,0.0110, (two-way mixed effects model with Geisser-Greenhouse correction with Tukey's multiple comparisons test). Dots present mean and error bars SEM. **c**, Frequency and **d**, total numbers of $CD19^+$ B cells in spleen (p-value < 0.0001) and brain with and without Rituximab treatment. **e**, Frequency of $CD20^+$ B cells in spleen (p-value = 0.0007) and brain (p-value = 0.0011) with and without Rituximab treatment. **f**, Total numbers of $CD20^+$ B cells in spleen (p-value = 0.0007) and brain (p-value = 0.0217) with and without Rituximab treatment. **g**, In vivo bioluminescence signal of perfused brains (PBS n = 5, EBV n = 4, Rituximab n = 7). **h**, Total numbers of $CD19^+CD11c^+$T-bet^+CXCR3^+ B cells in the blood (p-value < 0.0001), spleen (p-value = 0.0002), and brain (p-value = 0.0201) with and without Rituximab treatment (PBS n = 5, EBV n = 4, Rituximab n = 7). **i**, Total numbers of $CD4^+$ T cells in the brain with and without Rituximab treatment (EBV n = 4, Rituximab n = 7). **j**, Correlation between activated HLA-DR^+ $CD4^+$ T cells and T-bet^+CXCR3^+ B cells in the brains of EBV infected humanized mice. Solid line represents trend line obtained by linear regression, the dotted lines indicate 95% confidence bands (n = 12). **k**, Total numbers of $CD4^+$ T cell subtypes, including naïve ($CD45Ra^+CCR7^+$), effector memory ($CD45Ra^-CCR7^-$), central memory ($CD45Ra^-CCR7^+$) and Temra ($CD45Ra^+CCR7^-$) cells, with and without Rituximab treatment (EBV n = 4, Rituximab n = 7). a-k, were generated from 2 independent experiments with mice reconstituted from 2 different human $CD34^+$ hematopoietic progenitor cell donors. Unless otherwise indicated, p-values were calculated using the two-tailed MWU test. Error bar indicates SEM; each dot represents one single animal. *p < 0.05, **p < 0.01, ***p < 0.001, ****p < 0.0001.

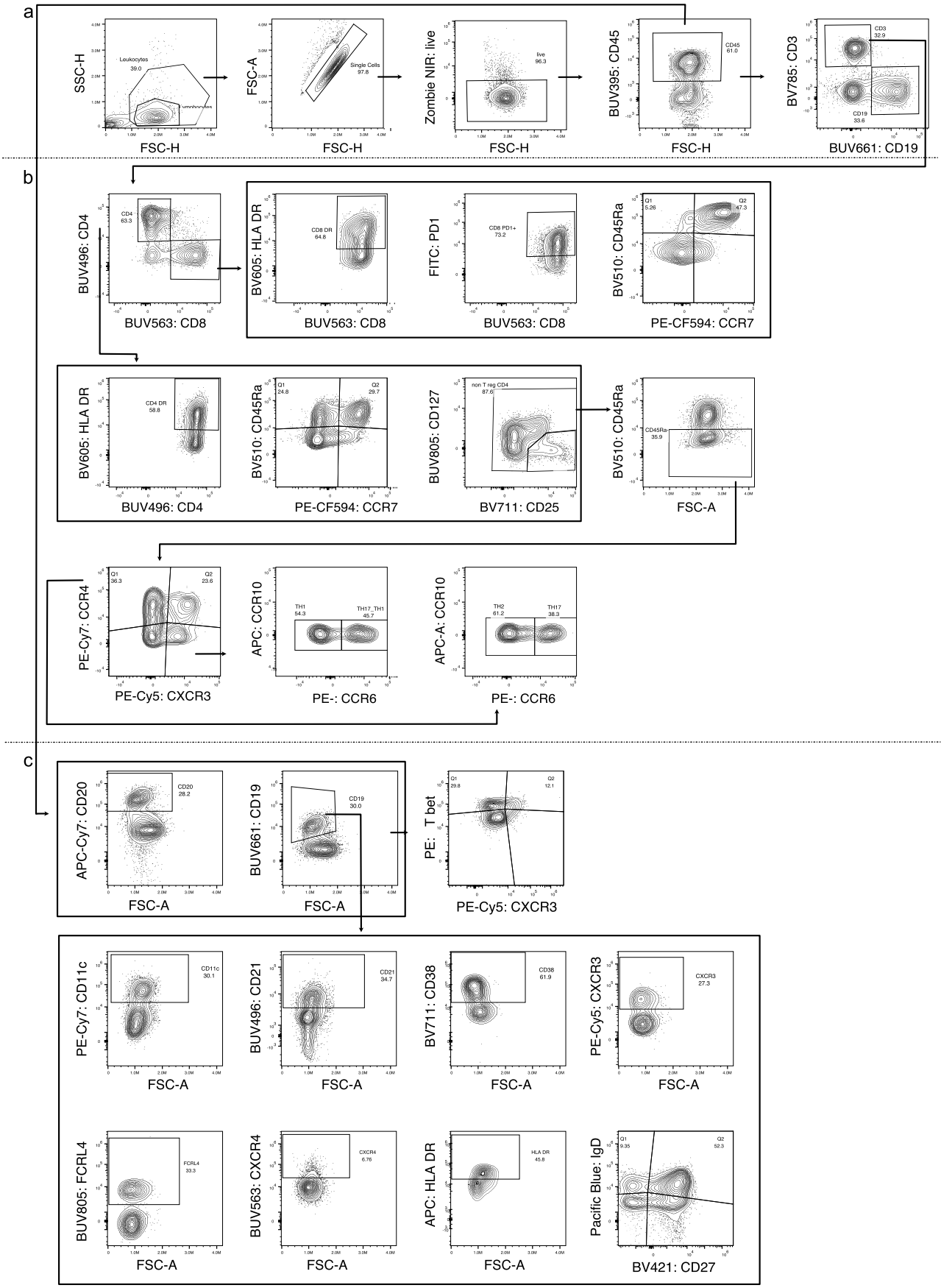

Extended Data Fig. 9 | See next page for caption.

Extended Data Fig. 9 | Gating strategy for human T and B cell populations ex vivo. a, Representative flow cytometric contour plots showing FACS gating strategy used for gating on lymphocytes, single cells, live cells and human $CD45^+$ cells followed by CD3 and CD19 gating. **b**, Representative flow cytometric contour plots following gating of Extended Data Fig. 9a for T cell populations. Depicted gating strategy was used for following FACS data panels: Fig. 1h–p and Fig. 5k–p and Extended Data Figs. 1g–p and 8i-k. **c**, Representative flow cytometric contour plots for gating of Extended Data Fig. 9a for B cell populations. Depicted gating strategy was used for following FACS data panels: Figs. 2a–d, 4e and 5b,c,h–j and Extended Data Figs. 1f, 2b–h, 7a,h,k and 7a–f,h.

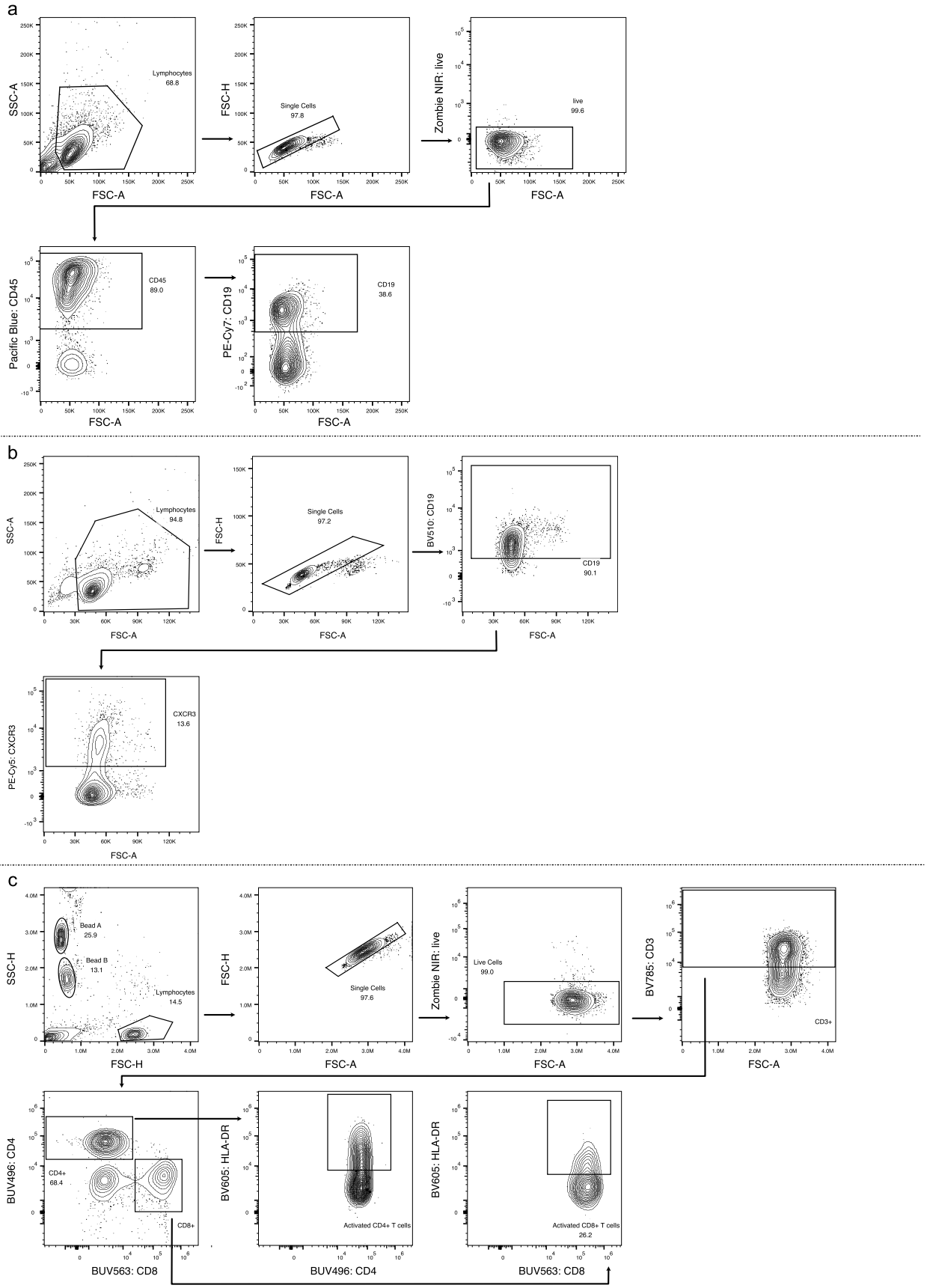

Extended Data Fig. 10 | Gating strategy for human T and B cell populations for in vitro experiments. a, Representative flow cytometric contour plots showing FACS gating strategy used for sorting CD19$^+$ B cells for data in Fig. 3 and Extended Data Figs. 4–6. **b**, Representative flow cytometric contour plots showing FACS gating strategy used for sorting CD19$^+$CXCR3$^+$ B cells for Extended Data Fig. 2g,h. **c**, Representative flow cytometric contour plots showing FACS gating strategy used for migration assays in Fig. 4h,i,k,l and Extended Data Fig. 7o–r,t.

nature portfolio

Corresponding author(s): Christian Münz

Last updated by author(s): Jun 23, 2025

Reporting Summary

Nature Portfolio wishes to improve the reproducibility of the work that we publish. This form provides structure for consistency and transparency in reporting. For further information on Nature Portfolio policies, see our Editorial Policies and the Editorial Policy Checklist.

Statistics

For all statistical analyses, confirm that the following items are present in the figure legend, table legend, main text, or Methods section.

n/a	Confirmed	
☐	☒	The exact sample size (*n*) for each experimental group/condition, given as a discrete number and unit of measurement
☐	☒	A statement on whether measurements were taken from distinct samples or whether the same sample was measured repeatedly
☐	☒	The statistical test(s) used AND whether they are one- or two-sided *Only common tests should be described solely by name; describe more complex techniques in the Methods section.*
☒	☐	A description of all covariates tested
☐	☒	A description of any assumptions or corrections, such as tests of normality and adjustment for multiple comparisons
☐	☒	A full description of the statistical parameters including central tendency (e.g. means) or other basic estimates (e.g. regression coefficient) AND variation (e.g. standard deviation) or associated estimates of uncertainty (e.g. confidence intervals)
☐	☒	For null hypothesis testing, the test statistic (e.g. *F*, *t*, *r*) with confidence intervals, effect sizes, degrees of freedom and *P* value noted *Give P values as exact values whenever suitable.*
☒	☐	For Bayesian analysis, information on the choice of priors and Markov chain Monte Carlo settings
☒	☐	For hierarchical and complex designs, identification of the appropriate level for tests and full reporting of outcomes
☐	☒	Estimates of effect sizes (e.g. Cohen's *d*, Pearson's *r*), indicating how they were calculated

Our web collection on statistics for biologists contains articles on many of the points above.

Software and code

Policy information about availability of computer code

Data collection	This study does not contain software and code for data collection.
Data analysis	R version 4.3.3 / 4.4.0, living image version 4.3.1 / 4.7, FlowJo Version 10.9.4, Phenochart version 2.2.0, InForm version 3.0.0, GraphPad Prism version 10.2.3, CRUSTY webtool (https://crusty.humanitas.it/), Basic version 1.2.0, ASHLAR version 1.18.0, QuPath version 0.4.3, FlowSOM version 2.10.0, MetaCyto version 1.24.0, Seurat version 5.1.0, Azimuth version 0.5.0, scRepertoire 2.0.4, UCell version 2.8.0, Slingshot version 2.12.0, ggplot2 version 3.5.1, RANN version 2.6.1, MISSILe 0.1.0, CellRanger version 7.2.0. Code used to analyse scRNAseq data and multiplex immunofluorescence images can be found via GitHub (https://github.com/EannaFennell/EBV-induces-CNS-homing-of-B-cells-attracting-inflammatory-T-cells). The package used for multiplex immunofluorescence analysis is also available from GitHub (https://github.com/EannaFennell/MISSILe).

For manuscripts utilizing custom algorithms or software that are central to the research but not yet described in published literature, software must be made available to editors and reviewers. We strongly encourage code deposition in a community repository (e.g. GitHub). See the Nature Portfolio guidelines for submitting code & software for further information.

Data

Policy information about availability of data

All manuscripts must include a data availability statement. This statement should provide the following information, where applicable:

- Accession codes, unique identifiers, or web links for publicly available datasets
- A description of any restrictions on data availability
- For clinical datasets or third party data, please ensure that the statement adheres to our policy

The single-cell RNA sequencing datasets analysed in this study are available from GEO (Fig. 3; GSE299939) and Zenodo (Extended Data Fig. 5; 10.5281/zenodo.15602185). The single-cell RNA sequencing was aligned to the GRCh38.p13 - Release 42 and EBV B95-8 genomes. The multiplex immunofluorescence images are also available to download from Zenodo (10.5281/zenodo.15599580).

Research involving human participants, their data, or biological material

Policy information about studies with human participants or human data. See also policy information about sex, gender (identity/presentation), and sexual orientation and race, ethnicity and racism.

Reporting on sex and gender	Lymphoblastoid cell lines created from healthy donor B cells (HD1, HD2) were collected from males. Human fetal liver samples contain donors from both sexes.
Reporting on race, ethnicity, or other socially relevant groupings	Geographic origin
Population characteristics	For LCL generation donors were chosen based on HLA-DRB1*15:01 expression. The donors were healthy (non-MS) Caucasian males between the ages of 25 and 55. No additional demographic or clinical information was accessible to the investigators. For CD34+ hematopoietic stem cells: No such data is available because all the samples were deposited without any identifying information. Buffy coat donors for migration assays: No such data is available because all the samples were deposited without any identifying information.
Recruitment	Healthy volunteers were selected based on suitable HLA type for lymphoblastoid cell line creation and human immune system reconstitution. These were either volunteers for blood donations of Blutspende Zürich, or procured via the non-profit Cercle Allocation Services Inc.
Ethics oversight	The following statement was now added to the manuscript: Blood samples of healthy volunteers were collected under the cantonal ethics committee (KEK) approved protocol with the BASEC-Nr. 2019-00837 with informed consent.

Note that full information on the approval of the study protocol must also be provided in the manuscript.

Field-specific reporting

Please select the one below that is the best fit for your research. If you are not sure, read the appropriate sections before making your selection.

☒ Life sciences ☐ Behavioural & social sciences ☐ Ecological, evolutionary & environmental sciences

For a reference copy of the document with all sections, see nature.com/documents/nr-reporting-summary-flat.pdf

Life sciences study design

All studies must disclose on these points even when the disclosure is negative.

Sample size	Sample size was determined based on the authors experience with similar in vivo experiments and was additionally dependent on the cohort size and human immune cell reconstitution level of the animals generated from one human hematopoietic progenitor cell donor. Sample sizes were calculated with a mixed effects model and F-tests (ANOVA) after defining fixed and rendom effects in the respective experiments. The effect size calculations were approved by the cantonal veterinary committee (KVET) prior to the start of the experimentation under protocol numbers ZH212/20 and ZH189/23. To ensure that observed effects were not donor-specific, each experiment was repeated with cells from at least two independent donors. The chosen sample sizes allowed for robust statistical analyses and produced reproducible outcomes. The exact number of animals used per experiment is specified in the figure legends.
Data exclusions	Only animals that survived to final timepoint of experiment were included. EBV injected mice were excluded from the dataset if they failed to show blood viral loads during the experiments. Rituximab treated mice were excluded from the dataset if their B cell counts after depletion were within or above the range of the mean + SEM of the EBV-infected control group.
Replication	The replication number for each experiment is indicated in the legend of the corresponding figure.

Randomization

Block randomization was used to distribute humanized mice to experimental groups under consideration of the sex and frequencies of reconstituted human cells in the peripheral blood prior to EBV infection, ensuring a similar sex-ratio and overall similar human immune cell reconstitution between the groups.

Blinding

The individual researchers were aware of the study design and blinding was not performed during in vivo experimentation, largely because experimental groups were macroscopically dinstinguishable (e.g. EBV infected versus PBS mice: weight loss and splenomegaly of infected mice). In addition, blinding was not feasible during the in vivo experiments, as the same researcher was responsible for the planning, execution, and monitoring of the mouse procedures, including infection and treatment. Awareness of the experimental design was necessary to ensure accurate timing, dosing, and animal welfare, which required consistent handling. Consequently, full blinding during the in vivo phase was not possible. However, in vitro assays derived from these experiments were performed under blinded conditions whenever feasible.

Reporting for specific materials, systems and methods

We require information from authors about some types of materials, experimental systems and methods used in many studies. Here, indicate whether each material, system or method listed is relevant to your study. If you are not sure if a list item applies to your research, read the appropriate section before selecting a response.

Materials & experimental systems

n/a	Involved in the study
☐	☒ Antibodies
☐	☒ Eukaryotic cell lines
☒	☐ Palaeontology and archaeology
☐	☒ Animals and other organisms
☒	☐ Clinical data
☒	☐ Dual use research of concern
☒	☐ Plants

Methods

n/a	Involved in the study
☒	☐ ChIP-seq
☐	☒ Flow cytometry
☒	☐ MRI-based neuroimaging

Antibodies

Antibodies used

Antibodies for flow cytometry
Antigen Conjugate Clone Source Cat# Final dilution
CD45 BUV3955 HI30 BD Bioscience 563791 1:100
CD4 BUV496 SIK1 BD Bioscience 612937 1:50
CD8 BUV563 RPA-T8 BD Bioscience 612914 1:100
CD19 BUV661 HIB19 BD Bioscience 741604 1:100
CD127 BUV805 HIL-7R-M21 BD Bioscience 748486 1:100
CD27 BV421 O323 Biolegend 302824 1:100
IgD PB IA6-3 Biolegend 348204 1:100
CD45Ra-BV510 HI100 Biolegend 304142 1:100
HLA-DR BV605 G46-6 Biolegend 307640 1:50
CD25 BV711 2A3 Biolegend 356138 1:50
CD3 BV785 OKT-3 Biolegend 317330 1:100
PD1 FITC EH12.2H7 Biolegend 329904 1:50
CD38 PerCP HIT2 Biolegend 303520 1:50
CCR6 PE 11A9 BD Bioscience 561019 1:50
CCR7 PE-CF594 GO4H7 BD Bioscience 562381 1:50
CXCR3 PE-Cy5 1C6/CXCR3 BD Bioscience 551128 1:50
CCR4 PE-Cy7 1G1 BD Bioscience 561034 1:50
CCR10 APC 1B5 BD Bioscience 564771 1:25
CD21 BUV496 B-ly4 BD Bioscience 750614 1:100
CD184 BUV563 15G5 BD Bioscience 741400 1:100
FCRL4-BUV805 A1 BD Bioscience 749182 1:100
CD38 BV711 HIT2 Biolegend 303528 1:100
T-bet PE ebio4B10 Thermo Fisher 12-5825-82 1:25
CD11c PE-Cy7 B-ly6 BD Bioscience 561356 1:100
HLA-DR APC L243 Biolegend 307610 1:100
CD20 APC-Cy7 2H7 Biolegend 302314 1:100
Isotype IgG1 PE MOPC-21 Biolegend 400112 1:25

For Chip Cytometry following antibodies were used
Antigen Conjugate Clone Source Cat# Final dilution
CD19 PE SJ25C1 Biolegend 363004 1:10
CD19 PE HIB19 Biolegend 302208 1:10
CXCR3 PE 1C6/CXCR3 BD Bioscience 560928 1:20
CD8 PerCP SK1 Biolegend 344708 1:20
CD39 FITC A1 Biolegend 328207 1:15
CD4 PerCP RPA-T4 Biolegend 300527 1:45
HLA-DR FITC G46.6 BD Bioscience 55581 1:120

CD11c PE 3.9 Biolegend 371504 1:400
CD20 (cytoplasmic)- PerCP 1412 Biolegend 340508 1:20
CD45 BUV395 HI30 BD Bioscience 563792 1:100
CD137 PE 4B4-1 Biolegend 309803 1:20
T-bet PE QA18A24 Biolegend 365904 1:20

Antibodies for multiplex dot-blot assay
Antigen Conjugate Clone Source Cat# Final dilution
His6-tagged human IgM Recombinant Human LMW IgM-Fc domain, Absolute Antibody, Pr00108-15.5 200 ng-1,56 ng
anti-His6 mouse monoclonal 3D5 IgG 6x-His Tag (C-term) Monoclonal Antibody 3D5 Thermo Fisher, R930-25 1:250 and 1:1000
anti-human IgM LI-COR® IRDye 800 polyclonal Biomol 609-145-007 1:10000
anti-mouse IgG LI-COR® IRDye 680 polyclonal Li-Cor 926-68070 1:10000

Antibodies for multiplex dot-blot assay
Antigen Clone Source Cat# Final dilution
EBNA2 PE2 Abcam ab90543 1:2000
EBV ZEBRA BZ1 Santa Cruz sc-53904 1:250
Mouse panCK polyclonal DAKO Z0622 1:500
MHC-II CR3/43 Abcam ab7856 1:250

Antibodies for light sheet microscopy
Antigen Conjugate Clone Source Cat# Final dilution
CD3 VioG570 REA613 REAfinity 130-133-790 1:50
CD45 VioR667 REA747 REAfinity 130-128-742 1:50
CD31 Vio780 REA784 REAfinity 130-135-521 1:50

Validation

All antibodies used were characterized and validated by providers hat are indicated in the field above at the respective dilutions for human lymphocyte or antibody stainings. His-tag antibody was validated by the laboratory of Dr. Josef Mautner to quantify spotted recombinant protein amounts in the described multiplex dot-plot assays.

Eukaryotic cell lines

Policy information about cell lines and Sex and Gender in Research

Cell line source(s)	Raji (ATCC CCL-86), EBV B95-8 (EBV-Luc) producer cells were kindly provided by Prof. Dr. Wolfgang Hammerschmidt (HelmholtzZentrum, Munich, Germany), lymphoblastoid cell lines were produced in house by EBV-Luc infection of purified human B cells, HEK293 cells were used to produce EBV infectious particles (293T, ATCC, CRL-3216).
Authentication	Authentication was not performed for this study.
Mycoplasma contamination	Cells have been routinely tested for mycoplasma and they were found negative.
Commonly misidentified lines (See ICLAC register)	No commonly misidentified cell lines were used.

Animals and other research organisms

Policy information about studies involving animals; ARRIVE guidelines recommended for reporting animal research, and Sex and Gender in Research

Laboratory animals	BALB/c Rag2-/- γc-/- hSIRPα transgenic HLA-DRB1*15:01 knock-in, HLA-A*02:01 knock-in hβ2m knock-in mice (BRGS-A2DR2; provided by Regeneron, Tarrytown, NE USA). NOD-scid IL2 receptor γ-chain deficient (NSG) (Jackson Laboratory, Bar Harbor, ME, USA). All mice used in the experiment and included in the analysis were between 3 and 8 months of age. Mice were housed in standard IVC type 2 long cages, accommodating up to five animals per cage. Standard enrichment was provided, including bedding, a red mouse house, tissue, and crinklets. The temperature was maintained between 21–24°C and humidity between 40–60%. Mice were exposed to a 12-hour dark/12-hour light cycle.
Wild animals	This study does not involve wild animals.
Reporting on sex	This study used both male and female mice.
Field-collected samples	This study does not invovle field collected animals.
Ethics oversight	All procedures were strictly performed in accordance with the animal protocols ZH 212/20 and ZH189/23, licensed by the veterinary office of the canton of Zurich (KVET), Switzerland.

Note that full information on the approval of the study protocol must also be provided in the manuscript.

Plants

Seed stocks	*Report on the source of all seed stocks or other plant material used. If applicable, state the seed stock centre and catalogue number. If plant specimens were collected from the field, describe the collection location, date and sampling procedures.*
Novel plant genotypes	*Describe the methods by which all novel plant genotypes were produced. This includes those generated by transgenic approaches, gene editing, chemical/radiation-based mutagenesis and hybridization. For transgenic lines, describe the transformation method, the number of independent lines analyzed and the generation upon which experiments were performed. For gene-edited lines, describe the editor used, the endogenous sequence targeted for editing, the targeting guide RNA sequence (if applicable) and how the editor was applied.*
Authentication	*Describe any authentication procedures for each seed stock used or novel genotype generated. Describe any experiments used to assess the effect of a mutation and, where applicable, how potential secondary effects (e.g. second site T-DNA insertions, mosiacism, off-target gene editing) were examined.*

Flow Cytometry

Plots

Confirm that:

☒ The axis labels state the marker and fluorochrome used (e.g. CD4-FITC).

☒ The axis scales are clearly visible. Include numbers along axes only for bottom left plot of group (a 'group' is an analysis of identical markers).

☒ All plots are contour plots with outliers or pseudocolor plots.

☒ A numerical value for number of cells or percentage (with statistics) is provided.

Methodology

Sample preparation	Spleen tissue was manually dissociated, filtered through 70-µm cell strainer, and subjected to Ficoll gradient centrifugation (Ficoll Paque Premiem, GE Healthcare). Whole blood was collected by tail-vein and terminal cardiac puncture in tubes containing heparin or EDTA. Prior to erythrocyte lysis by ACK lysis buffer. Brain tissue was digested using the gentleMACS (Miltenyi) following 30min at 37°C in buffer containing DNase and collagenase, followed by filtering and separation of lymphocytes on Percoll gradients.
Instrument	Flow cytometry was peformed on FACS BD Canto (BD Biosciences) and Spectral analyzer Aurora (Cytek).
Software	FlowJo V10 was used to analyze FACS data or the CRUSTY webtool (https://crusty.humanitas.it/).
Cell population abundance	Quantification of cell populations are provided as total number of tissue or percentage of referenced population as described in the figure and figure legends.
Gating strategy	For all experiments, cells were first identified by SSC-A/FSC-A scatter gating and single cells based on SSC-H/SSC-A and FSC-H/FCS-A. Dead cells were then excluded based on the absence of fixable live/dead viability dye. Human immune cells were then identified by the positive staining for human CD45. Detailed gating strategies for specific cell populations are provided in the Extended Data Figures.

☒ Tick this box to confirm that a figure exemplifying the gating strategy is provided in the Supplementary Information.